

<sup>1</sup>  
<sup>2</sup> Susceptible host dynamics explain pathogen resilience to  
<sup>3</sup> perturbations

<sup>4</sup>  
<sup>5</sup> Sang Woo Park<sup>1,\*</sup> Bjarke Frost Nielsen<sup>2</sup> Emily Howerton<sup>2</sup> Bryan T. Grenfell<sup>2,3,4</sup>  
<sup>6</sup> Sarah Cobey<sup>1</sup>

<sup>7</sup> **1** Department of Ecology and Evolution, University of Chicago, Chicago, IL, USA

<sup>8</sup> **2** Department of Ecology and Evolutionary Biology, Princeton University,  
Princeton, NJ, USA

<sup>10</sup> **3** High Meadows Environmental Institute, Princeton University, Princeton, NJ,  
<sup>11</sup> USA

<sup>12</sup> **4** Princeton School of Public and International Affairs, Princeton, NJ, USA

<sup>13</sup> \*Corresponding author: swp2@uchicago.edu

## <sup>14</sup> **Abstract**

<sup>15</sup> Interventions to slow the spread of SARS-CoV-2 significantly disrupted the transmission  
<sup>16</sup> of other pathogens. As interventions lifted, whether and when human pathogens  
<sup>17</sup> would eventually return to their pre-pandemic dynamics remains to be answered.  
<sup>18</sup> Here, we present a framework for estimating pathogen resilience based on how fast  
<sup>19</sup> epidemic patterns return to their pre-pandemic dynamics. By analyzing time series  
<sup>20</sup> data from Hong Kong, Canada, Korea, and the US, we quantify the resilience of  
<sup>21</sup> common respiratory pathogens and further predict when each pathogen will eventually  
<sup>22</sup> return to its pre-pandemic dynamics. Our predictions are able to distinguish  
<sup>23</sup> which pathogens should have returned already, and deviations from these predictions  
<sup>24</sup> reveal long-term impacts of pandemic perturbations. We find a faster rate of  
<sup>25</sup> susceptible replenishment underlies pathogen resilience and sensitivity to both large  
<sup>26</sup> and small perturbations. Overall, our analysis highlights the persistent nature of  
<sup>27</sup> common respiratory pathogens compared to vaccine-preventable infections, such as  
<sup>28</sup> measles.

## <sup>29</sup> **Significance Statement**

<sup>30</sup> The COVID-19 interventions slowed down the transmission of other respiratory  
<sup>31</sup> pathogens, raising questions about mechanisms driving differences in responses to  
<sup>32</sup> COVID-19 intervention measures. To address this gap, we seek to characterize the  
<sup>33</sup> pathogen resilience to perturbations by quantifying how fast each pathogen returns  
<sup>34</sup> to its pre-pandemic epidemic cycles. We apply the resulting framework to data  
<sup>35</sup> from Hong Kong, Canada, Korea, and the US, and show that common respiratory  
<sup>36</sup> pathogens are much more resilient than vaccine-preventable infections, like measles.

<sup>37</sup> Finally, we show that how fast the susceptible population becomes replenished—  
<sup>38</sup> for example, through waning immunity—is a key determinant for how resilient a  
<sup>39</sup> pathogen is to perturbations, including large interventions and small stochastic  
<sup>40</sup> changes in the dynamics.

# 41 Introduction

42 Non-pharmaceutical interventions to slow the spread of SARS-CoV-2 disrupted the  
 43 transmission of other human respiratory pathogens, adding uncertainties to their future  
 44 epidemic dynamics and their public health burden [1]. As interventions lifted,  
 45 large heterogeneities in outbreak dynamics were observed across different pathogens  
 46 in different countries, with some pathogens exhibiting earlier and faster resurgences  
 47 than others [2, 3, 4]. Heterogeneities in the overall reduction in transmission and the  
 48 timing of re-emergence likely reflect differences in intervention patterns, pathogen  
 49 characteristics, immigration/importation from other countries, and pre-pandemic  
 50 pathogen dynamics [5]. Therefore, comparing the differential impact of the pandemic  
 51 perturbations across pathogens can provide unique opportunities to learn about underly-  
 52 ing pathogen characteristics across different populations, such as their trans-  
 53 missibility or duration of immunity, from heterogeneities in re-emergence patterns  
 54 [6].

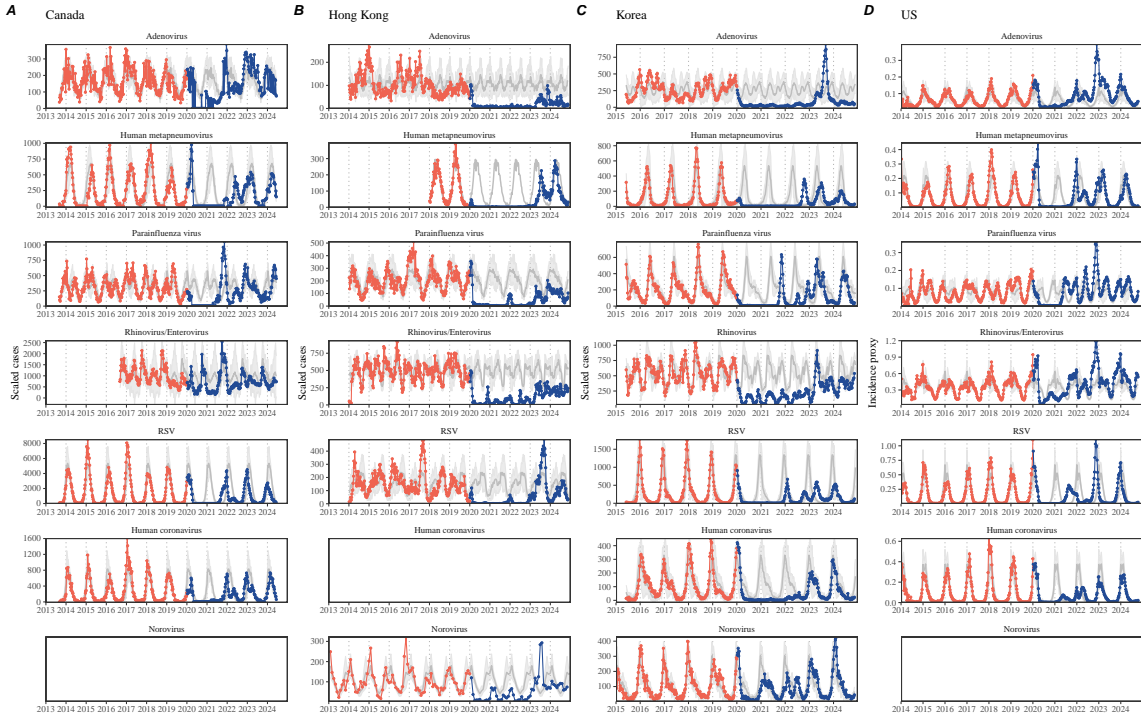


Figure 1: **Observed heterogeneity in responses to pandemic perturbations across respiratory pathogens and norovirus in (A) Canada, (B) Hong Kong, (C) Korea, and (D) US.** Red points and lines represent data before 2020. Blue points and lines represent data since 2020. Gray lines and shaded regions represent the mean seasonal patterns and corresponding 95% confidence intervals around the mean. Mean seasonal patterns were calculated by aggregating cases before 2020 into 52 weekly bins and taking the average in each week. Cases were scaled to account for changes in testing patterns (Materials and Methods).

55 Even though more than five years have passed since the emergence of SARS-CoV-  
56 2, we still observe persistent changes in pathogen dynamics following the pandemic  
57 perturbations. For example, compared to pre-pandemic, seasonal patterns, human  
58 metapneumovirus in Korea seems to circulate at lower levels, whereas RSV in Ko-  
59 rea seems to exhibit different seasonality (Figure 1). These observations suggest  
60 the possibility of a long-term change in pathogen dynamics following the pandemic  
61 perturbations, which might be driven by a long-term shift in human behavior or  
62 population-level immunity [7, 8]. For example, the emergence of SARS-CoV-2 could  
63 have caused a long-term shift in population-level immunity through its interactions  
64 with other pathogens [9], especially with seasonal coronaviruses [7, 10, 11]. The pos-  
65 sibility of a long-lasting impact of the pandemic perturbations poses an important  
66 question for future infectious disease dynamics: can we predict whether and when  
67 other pathogens will eventually return to their pre-pandemic dynamics?

68 So far, most analyses of respiratory pathogens after pandemic perturbations have  
69 focused on characterizing the timing of rebound [1, 12, 5]. Instead, we seek to char-  
70 acterize how fast (and whether) a pathogen returns to its pre-pandemic dynamics.  
71 These two concepts have a subtle but important difference. For example, it took  
72 more than 3 years for human metapneumovirus to rebound in Hong Kong, but the  
73 observed epidemic patterns in 2024 appear similar to the pre-pandemic seasonal  
74 mean, suggesting a possible return to pre-pandemic dynamics, though confirmation  
75 may require multiple seasons (Figure 1). Measuring this rate of return is useful be-  
76 cause it allows us to quantify the ecological resilience of a host-pathogen system,  
77 which can inform responses to future interventions [13, 14, 15, 16].

78 In this study, we lay out theoretical and statistical approaches to characterizing  
79 the resilience of a host-pathogen system based on how fast the system recovers from  
80 perturbation. We begin by laying out a few representative scenarios that capture  
81 the potential impact of pandemic perturbations on endemic pathogen dynamics and  
82 illustrate how resilience can be measured by comparing the pre- and post-pandemic  
83 dynamics of susceptible and infected hosts. In practice, information on susceptible  
84 hosts is often unavailable, making this theoretical approach infeasible. Instead, we  
85 utilize a mathematical technique to reconstruct attractors from the data [17], which  
86 allows us to measure the rate at which the host-pathogen system approaches this  
87 empirical attractor after a perturbation; we define this rate to be the empirical  
88 resilience of the host-pathogen system. We use this method to analyze pathogen  
89 surveillance data for respiratory and non-respiratory pathogens from Canada, Hong  
90 Kong, Korea, and the US. Finally, we show that susceptible host dynamics explain  
91 variation in pathogen resilience and demonstrate that more resilient pathogens will be  
92 less sensitive to perturbations caused by demographic stochasticity, thereby providing  
93 a direct link between pathogen resilience and persistence.

## <sup>94</sup> Conceptual introduction to pathogen resilience

<sup>95</sup> In the classical ecological literature, the resilience of an ecological system is measured  
<sup>96</sup> by the rate at which the system returns to its reference state following a perturbation  
<sup>97</sup> [13, 14, 15, 16]. This rate corresponds to the largest real part of the eigenvalues of  
<sup>98</sup> the linearized system near equilibrium—here, we refer to this value as the *intrinsic*  
<sup>99</sup> resilience of the system, which represents the expected rate of return from perturbed  
<sup>100</sup> states. In practice, we rarely know the true model describing the dynamics of com-  
<sup>101</sup> mon respiratory pathogens, limiting our ability to infer the intrinsic resilience of a  
<sup>102</sup> system. Instead, we can measure the *empirical* resilience of a host-pathogen system  
<sup>103</sup> by looking at how fast the system returns to the pre-perturbation endemic dynamics  
<sup>104</sup> after the perturbation has ended. The COVID-19 pandemic provides a crucial exam-  
<sup>105</sup> ple of a major perturbation, providing unique opportunities to measure the resilience  
<sup>106</sup> of a host-pathogen system across different countries.

<sup>107</sup> **Resilience of a single-strain system under a short-term perturbation.**  
<sup>108</sup> As an example, we begin with a simple Susceptible-Infected-Recovered-Susceptible  
<sup>109</sup> (SIRS) model with seasonally forced transmission and demography (i.e., birth and  
<sup>110</sup> death). The SIRS model is the simplest model that allows for the waning of immunity  
<sup>111</sup> and is commonly used for modeling the dynamics of respiratory pathogens [18]. First,  
<sup>112</sup> consider a pandemic perturbation that reduces transmission by 50% for 6 months  
<sup>113</sup> starting in 2020, which causes epidemic patterns to deviate from their original stable  
<sup>114</sup> annual cycle for a short period of time and eventually come back (Figure 2A). To  
<sup>115</sup> measure the resilience of this system empirically, we first need to be able to measure  
<sup>116</sup> the distance from its pre-pandemic attractor, which is defined as a set of points in  
<sup>117</sup> state space or phase plane that the system is pulled towards [19]. There are many  
<sup>118</sup> ways we can measure the distance from the attractor, but for illustrative purposes, we  
<sup>119</sup> choose one of the most parsimonious approaches: we look at how the susceptible (S)  
<sup>120</sup> and infected (I) populations change over time and measure the Euclidean distance on  
<sup>121</sup> the SI phase plane, using the counterfactual unperturbed phase plane as a reference  
<sup>122</sup> (Figure 2B; Materials and Methods). In this simple case, the locally estimated  
<sup>123</sup> scatterplot smoothing (LOESS) fit indicates that the distance from the attractor  
<sup>124</sup> decreases exponentially (linearly on a log scale) with time on average (Figure 2C).  
<sup>125</sup> Furthermore, the overall rate of return approximates the intrinsic resilience of the  
<sup>126</sup> seasonally unforced system (Figure 2C).

<sup>127</sup> **Resilience of a single-strain system under a long-term perturbation.**  
<sup>128</sup> Alternatively, pandemic perturbations can have a lasting impact on the forces driv-  
<sup>129</sup> ing pathogen dynamics through a long-term reduction in transmission or permanent  
<sup>130</sup> change in immunity. As an example, we consider a scenario in which a 10% reduc-  
<sup>131</sup> tion in transmission persists even after the major pandemic perturbations are lifted  
<sup>132</sup> (Figure 2D–F). In such cases, we cannot know whether the pathogen will return to  
<sup>133</sup> its original cycle or a different cycle until many years have passed, and we cannot  
<sup>134</sup> a priori measure the distance to the new unknown attractor that the system might  
<sup>135</sup> eventually approach. Nonetheless, we can still measure the distance from the pre-

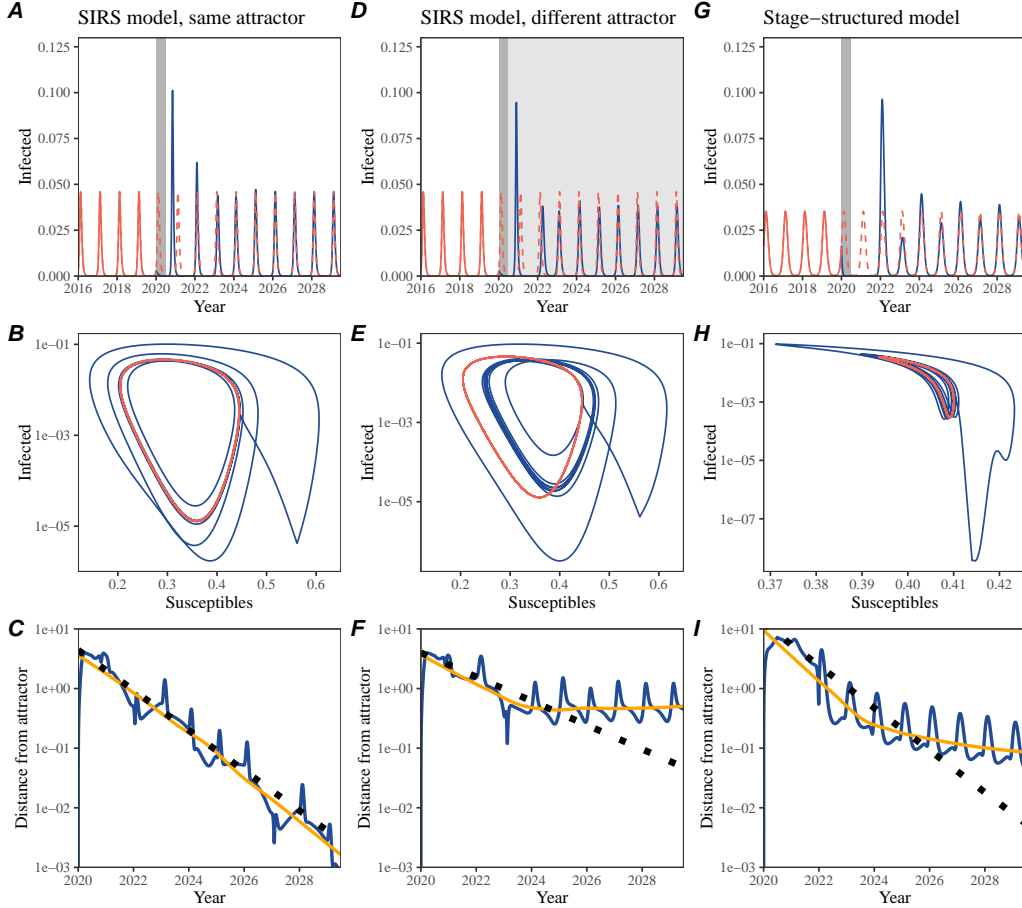


**Figure 2: A simple method to measure pathogen resilience following pandemic perturbations across different scenarios.** (A, D, G) Simulated epidemic trajectories across various models. Red and blue solid lines represent epidemic dynamics before and after pandemic perturbations are introduced, respectively. Red dashed lines represent counterfactual epidemic dynamics in the absence of perturbations. Gray regions indicate the duration of perturbations with the dark gray region representing a 50% transmission reduction and the light gray region representing a 10% transmission reduction. (B, E, H) Phase plane representation of the time series in panels A, D, and G alongside the corresponding susceptible host dynamics. Red and blue solid lines represent epidemic trajectories on an SI phase plane before and after perturbations are introduced, respectively. (C, F, I) Changes in distance from the attractor over time on a log scale. Blue lines represent the distance from the attractor. Orange lines represent the locally estimated scatterplot smoothing (LOESS) fits to the logged distance from the attractor. Dotted lines show the intrinsic resilience of the seasonally unforced system.

136 pandemic attractor and ask how the distance changes over time (Figure 2E). The  
137 LOESS fit suggests that the distance from the pre-pandemic attractor will initially  
138 decrease exponentially on average (equivalently, linearly on a log scale) and even-  
139 tually plateau (Figure 2F). Here, a permanent 10% reduction in transmission rate  
140 slows the system, which causes the distance from the pre-pandemic attractor initially  
141 to decrease at a slower rate (Figure 2F) than it would have otherwise (Figure 2C)  
142 before plateauing at a fixed distance between the two attractors. This example shows  
143 that resilience is not necessarily an intrinsic property of a specific pathogen. Instead,  
144 pathogen resilience is a property of a specific attractor that a host-pathogen system  
145 approaches, which depends on both pathogen and host characteristics.

146 **Resilience of a single-strain system with long-term transients.** Finally,  
147 transient phenomena can further complicate the picture (Figure 2G–I). For exam-  
148 ple, a stage-structured model that accounts for reduction in secondary susceptibility  
149 initially exhibits a stable annual cycle, but perturbations from a 10% reduction in  
150 transmission for 6 months cause the epidemic to shift to biennial cycles (Figure 2G).  
151 The system eventually approaches the original pre-pandemic attractor (Figure 2H),  
152 suggesting that this biennial cycle is a transient. The LOESS fit indicates that the  
153 distance from the attractor initially decreases exponentially at a rate that is consis-  
154 tent with the intrinsic resilience of the seasonally unforced stage-structured system,  
155 but the approach to the attractor slows down with the damped oscillations (Figure  
156 2I). This behavior is also referred to as a ghost attractor, which causes long tran-  
157 sient dynamics and slow transitions [20]. Strong seasonal forcing in transmission can  
158 also lead to transient phenomena for a simple SIRS model, causing a slow return to  
159 pre-perturbation dynamics (Supplementary Figure S1).

160 **Resilience of a two-strain system.** This empirical approach allows us to  
161 measure the resilience of a two-strain host-pathogen system as well even when we  
162 have incomplete observation of the infection dynamics. Simulations from a simple  
163 two-strain competition system illustrate that separate analyses of individual strain  
164 dynamics (e.g., RSV subtype A vs B) and a joint analysis of total infections (e.g.,  
165 total RSV infections) yield identical resilience estimates (Supplementary Figure S2,  
166 3). This is expected because eigenvalues determine the dynamics of the entire system  
167 around the equilibrium, meaning that both strains should exhibit identical rates of  
168 return following a perturbation. Analogous to a single-strain system, strong sea-  
169 sonal forcing in transmission can cause the two-strain system to slow down through  
170 transient phenomena (Supplementary Figure S4).

171 These observations yield three insights. First, we can directly estimate the empi-  
172 rical resilience of a host-pathogen system by measuring the rate at which the system  
173 approaches an attractor, provided that we have a way to quantify the distance from  
174 the attractor—as we discuss later, the attractor of a system can be reconstructed  
175 from data from mathematical theory without making assumptions about the under-  
176 lying model. The empirical approach to estimating pathogen resilience is particularly  
177 convenient because it does not require us to know the true underlying model; esti-  
178 mating the intrinsic resilience from fitting misspecified models can lead to biased

estimates (Supplementary Figure S5). Second, resilience estimates allow us to make phenomenological predictions about the dynamics of a host-pathogen system following a perturbation. Assuming that an attractor has not changed and the distance from the attractor will decrease exponentially over time, we can estimate when the system should reach an attractor. Finally, a change in the (exponential) rate of approach can provide information about whether the system has reached an alternative attractor, or a ghost attractor, that is different from the original, pre-pandemic attractor. These alternative attractors may reflect permanent changes in transmission patterns as well as changes in immune landscapes. There will be periods of time when it is difficult to tell whether pathogen dynamics are still diverging from the original attractor due to a long-term perturbation, or have entered the basin of attraction of a new attractor. Now that several years have passed since major interventions have been lifted, many respiratory pathogens may have had sufficient time to begin returning to their post-intervention attractors—empirical comparisons between current cases and pre-pandemic cases are consistent with this hypothesis (Figure 1). With recent data, we can start to evaluate whether we see early signs of convergence to the former attractor or a new one.

## Inferring pathogen resilience from real data

Based on these patterns, we now lay out our approach to estimating pathogen resilience from real data (Figure 3). We first tested this approach against simulations and applied it to real data. Specifically, we analyzed case time series of respiratory pathogens from four countries: Canada, Hong Kong, Korea, and the US.

So far, we have focused on simple examples that assume a constant transmission reduction during the pandemic. However, in practice, the impact of pandemic perturbations on pathogen transmission is likely more complex (Figure 3A), reflecting the introduction and relaxation of various intervention strategies. In some cases, strong perturbations likely caused local fadeouts, requiring immigration/importation from another location for epidemic rebound. Such complexities could lead to longer delays between the introduction of pandemic perturbations and pathogen rebound as well as temporal variation in outbreak sizes (Figure 3B); in this example, continued transmission reduction from interventions limits the size of the first outbreak in 2021 following the rebound, allowing for a larger outbreak in 2022 when interventions are further relaxed.

Previously, we relied on the dynamics of susceptible and infected hosts to compute the distance from the attractor (Figure 2), but information on susceptible hosts is rarely available in practice. In addition, uncertainties in case counts due to observation error, strain evolution, and multiannual cycles in the observed epidemic dynamics (e.g., adenovirus circulation patterns in Hong Kong and Korea) add challenges to defining pre-pandemic attractors, which limits our ability to measure the distance from the attractor. To address these challenges, we can reconstruct an em-

219 empirical attractor by utilizing Takens' theorem [17], which states that an attractor of a  
220 nonlinear multidimensional system can be mapped onto a delayed embedding (Materials  
221 and Methods). For example, we can use delayed logged values of pre-pandemic  
222 cases  $C(t)$  (Figure 3C) to reconstruct the attractor:

$$\langle \log(C(t) + 1), \log(C(t - \tau) + 1), \dots, \log(C(t - (M - 1)\tau) + 1) \rangle, \quad (1)$$

223 where the delay  $\tau$  and embedding dimension  $M$  are determined based on autocor-  
224 relations and false nearest neighbors, respectively [21, 22]. This allows us to define  
225 the pre-pandemic attractor as a points on an  $M$ -dimensional space. We can then  
226 apply the same delay and embedding dimensions to the entire time series to deter-  
227 mine the position in multi-dimensional state space (Figure 3D), which allows us to  
228 measure the nearest neighbor distance between the current state of the system and  
229 the empirical pre-pandemic attractor (Figure 3E). Specifically, the nearest neighbor  
230 distance is calculated by computing the distance between the current position on  
231 the  $M$ -dimensional space and all points in the empirical attractor set and taking the  
232 minimum value. In theory, we can now quantify how fast this distance decreases by  
233 fitting a linear regression on a log scale, where the slope of the linear regression em-  
234 pirically measures pathogen resilience, with a steeper slope corresponding to a higher  
235 resilience estimate (Figure 3E). However, resulting estimates of pathogen resilience  
236 can be sensitive to choices about embedding delays and dimensions. For example,  
237 using longer delays and higher dimensions tends to smooth out temporal variations  
238 in the distance from the attractor (Supplementary Figure S6).

239 Complex changes in the distance from the attractor suggest that estimating  
240 pathogen resilience from linear regression will be particularly sensitive to our choice  
241 of fitting windows for the regression (Figure 3E). Therefore, before we tried estimat-  
242 ing resilience from real data, we explored an automated window selection criteria  
243 for linear regression and tested it against randomized, stochastic simulations across  
244 a range of realistic pandemic perturbation shapes. In doing so, we also explored  
245 optimal choices for embedding dimensions and evaluated our choices of fitting win-  
246 dows parameters and embedding dimensions by quantifying correlation coefficients  
247 between the estimated resilience and the intrinsic resilience of a seasonally unforced  
248 system (Materials and Methods). Overall, we found large variation in estimation  
249 performances with correlation coefficients ranging from 0.21 to 0.61 (Supplementary  
250 Figure S7). In almost all cases, the automated window selection approach outper-  
251 formed a naive approach, which performs regression using all data from the the  
252 timing of peak distance to current time (Supplementary Figure S7).

253 Based on the best-performing window selection criteria and embedding dimen-  
254 sion, we applied this approach to pathogen surveillance data presented in Figure  
255 1 (Materials and Methods). For each time series, we applied Takens' theorem in-  
256 dependently to reconstruct the empirical attractor and obtained the corresponding  
257 time series of distances from attractors (Supplementary Figure S8). Then, we used  
258 the automated window selection criteria to fit a linear regression and estimated the  
259 empirical resilience for each pathogen in each country (Supplementary Figure S8);

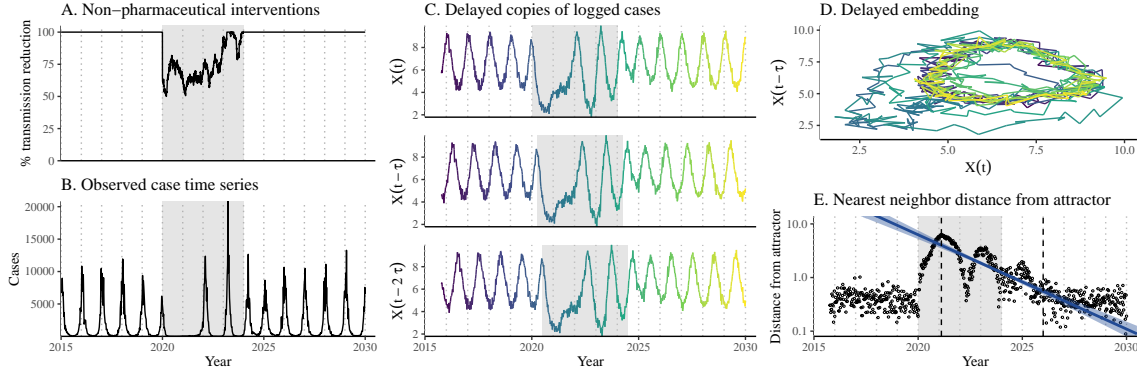


Figure 3: **A schematic diagram explaining the inference of pathogen resilience from synthetic data.** (A) A realistic example of simulated pandemic perturbations, represented by a relative reduction in transmission. (B) The impact of the synthetic pandemic perturbation on epidemic dynamics simulated using a SIRS model with demographic stochasticity. (C) Generating delayed copies of the logged time series allows us to obtain an embedding. (D) Two dimensional representation of an embedding. (E) Delayed embedding allows us to calculate the nearest neighbor distance from the empirical attractor, which is determined based on the pre-pandemic time series. Blue lines and dashed regions represent the linear regression fit and the associated 95% confidence interval. This distance time series can be used to infer pathogen resilience after choosing an appropriate window for linear regression. For illustration purposes, an arbitrary fitting window was chosen.

the window selection criteria gave poor regression windows in three cases (norovirus in Hong Kong and Korea and rhinovirus/enterovirus in the US), leading to unrealistically low resilience estimates, and so we used ad-hoc regression windows instead (Supplementary Figure S9; Materials and Methods).

For all pathogens we considered, resilience estimates fall between 0.4/year and 1.8/year (Figure 4A). We estimated the mean resilience of common respiratory pathogens to be 0.99/year (95% CI: 0.81/year–1.18/year). For reference, this is  $\approx 7.5$  times higher than the intrinsic resilience of pre-vaccination measles in England and Wales ( $\approx 0.13/\text{year}$ ). Finally, resilience estimates for norovirus, a gastrointestinal pathogen, were comparable to those of common respiratory pathogens: 1.44/year (95% CI: 1.01/year–1.87/year) for Hong Kong and 1.07/year (95% CI: 0.86/year–1.29/year) for Korea. Based on a simple ANOVA test, we did not find significant differences in resilience estimates across countries ( $p = 0.25$ ) or pathogens ( $p = 0.67$ ).

Using resilience estimates, we predicted when each pathogen would hypothetically return to their pre-pandemic dynamics, assuming no long-term change in the attractor. Specifically, we extended our linear regression fits to distance-from-attractor time series and ask when the predicted regression line will cross a threshold value; since we relied on nearest neighbor distances, pre-pandemic distances are always greater than zero (Figure 3E), meaning that we can use the mean of pre-pandemic

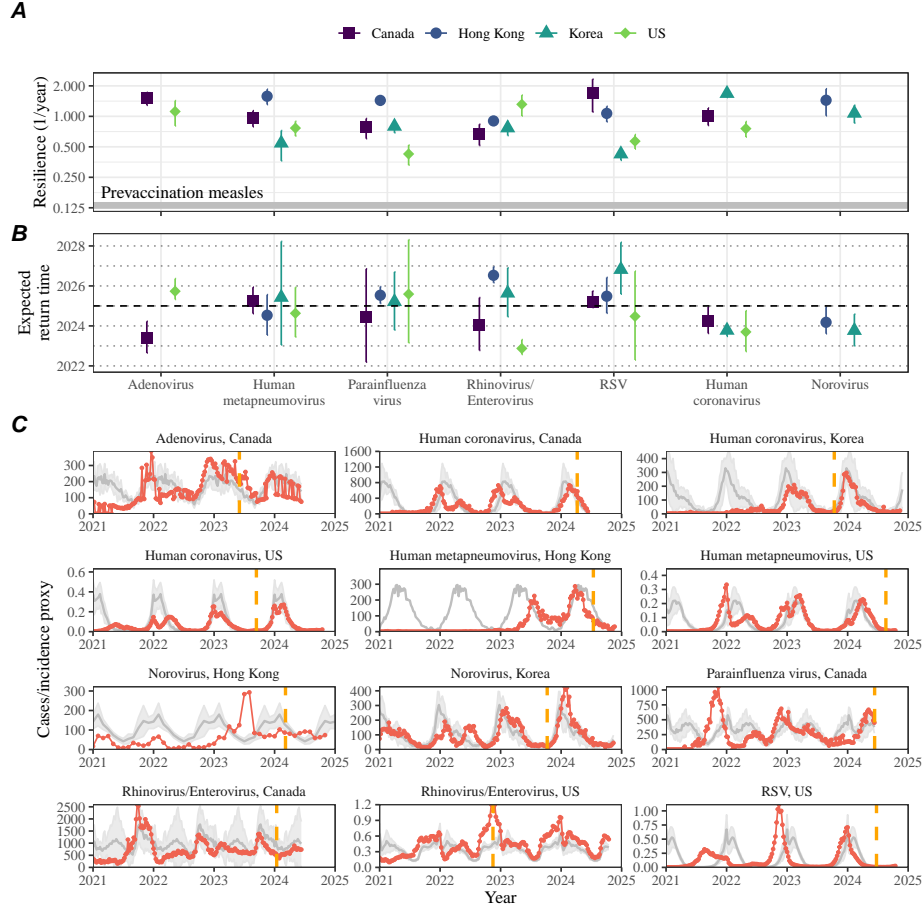


Figure 4: **Summary of resilience estimates and predictions for return time.** (A) Estimated pathogen resilience. The gray horizontal line represents the intrinsic resilience of pre-vaccination measles dynamics. (B) Predicted timing of when each pathogen will return to their pre-pandemic cycles. The dashed line in panel B indicates the end of 2024. Error bars represent 95% confidence intervals. (C) Observed dynamics for pathogen that are predicted to have returned before the end of 2024. Red points and lines represent data before 2020. Gray lines and shaded regions represent the mean seasonal patterns and corresponding 95% confidence intervals around the mean, previously shown in Figure 1. Orange vertical lines represent the predicted timing of return.

279 distances as our threshold.

280 We predicted that a return to pre-pandemic cycles has occurred or would be  
 281 imminent for most pathogens (Figure 4B). In particular, we predicted that 12 out  
 282 of 23 pathogen-country pairs should have already returned before the end of 2024.  
 283 For almost all pathogens that were predicted to have returned already, the observed  
 284 epidemic dynamics showed clear convergence towards their pre-pandemic seasonal

averages, confirming our predictions (Figure 4C). However, there were a few exceptions, including norovirus in Hong Kong and rhinovirus/enterovirus in the US, where the observed epidemic dynamics in 2024 exhibit clear deviation from their pre-pandemic seasonal averages (Figure 4C; Figure S9). These observations suggest a possibility that some common respiratory pathogens may have converged to different attractors or are still exhibiting non-equilibrium dynamics. In contrast, pathogens that were predicted to have not returned yet also showed clear differences from their pre-pandemic seasonal averages; as many of these pathogens are predicted to return in 2025–2026, we may be able to test these predictions in near future (Supplementary Figure S10). Our reconstructions of distance time series and estimates of pathogen resilience and expected return time were generally robust to choices of embedding dimensions (Supplementary Figure S11–12).

To evaluate the ability of our approach to make out-of-sample predictions, we applied our framework to the same data set using observations up to the 26th week of 2023 (Supplementary Figure S13–14). Limiting the data led to greater uncertainty in resilience estimates and corresponding predictions for the expected return time (Supplementary Figure S14A,B). The expected and observed return times exhibit weak positive correlation ( $\rho = 0.36$ ; 95% CI: -0.34–0.81), and 7 out of 10 confidence intervals contain the true value (Supplementary Figure S14C). We found moderate correlations ( $\rho = 0.51$ ; 95% CI: 0.01–0.80) in predictions for the expected return time between partial regression fits, which rely on observations up to the 26th week of 2023, and full regression fits, which rely on the entire data set (Supplementary Figure S14D); this implies consistency in our predictions. However, resilience estimates from partial regression fits and full regression fits were weakly correlated ( $\rho = 0.30$ ; 95% CI: -0.23–0.70), implying challenges in estimating pathogen resilience from limited data (Supplementary Figure S14E).

## Susceptible host dynamics explain variation in pathogen resilience

So far, we have focused on quantifying pathogen resilience from the observed patterns of pathogen re-emergence following pandemic perturbations. But what factors determine the resilience of a host-pathogen system? To address this question, we used the SIRS model to explore how changes in susceptible host dynamics affect pathogen resilience. To do so, we varied the basic reproduction number  $\mathcal{R}_0$ , which represents the average number of secondary infections caused by a newly infected individual in a fully susceptible population, and the duration of immunity and computed intrinsic resilience for each parameter.

We found that an increase in  $\mathcal{R}_0$  and a decrease in the duration of immunity correspond to an increase in pathogen resilience (Figure 5A). Similarly, an increase in  $\mathcal{R}_0$  and a decrease in the duration of immunity corresponds to a faster per-capita rate of susceptible replenishment, which is defined as the ratio between absolute

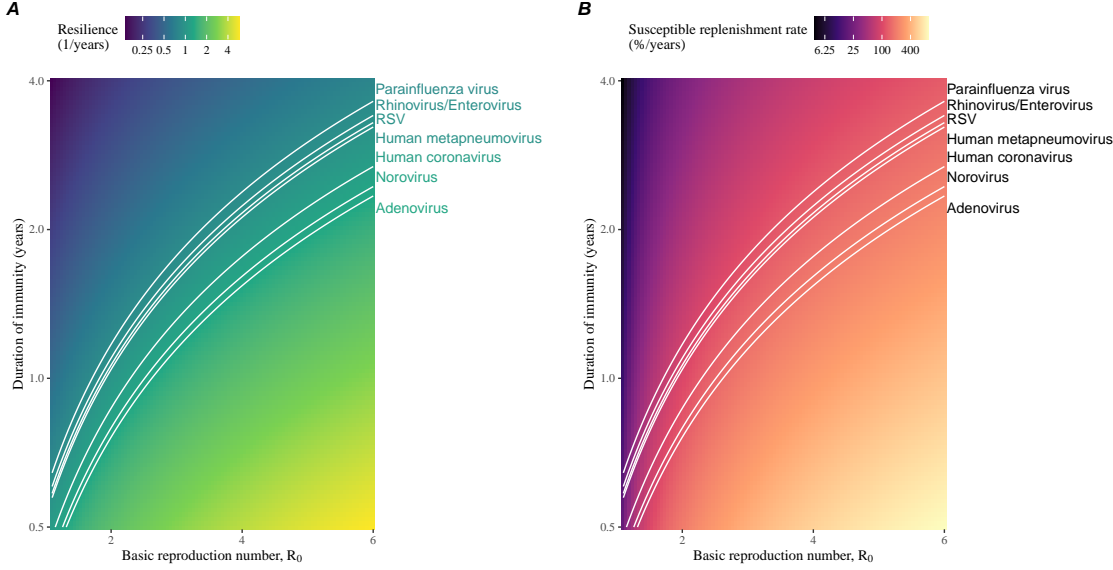


**Figure 5: Linking pathogen resilience to epidemiological parameters and susceptible host dynamics.** (A) Intrinsic resilience as a function of the basic reproduction number  $\mathcal{R}_0$  and the duration of immunity. (B) Per-capita susceptible replenishment rate as a function of the basic reproduction number  $\mathcal{R}_0$  and the duration of immunity. The standard SIRS model without seasonal forcing is used to compute intrinsic resilience and the per-capita susceptible replenishment rate. Lines correspond to a set of parameters that are consistent with mean resilience estimates for each pathogen, averaged across different countries.

rate at which new susceptibles enter the population and the equilibrium number of susceptible individuals in the population,  $S^*$  (Figure 5B). We note that a higher  $\mathcal{R}_0$  drives a faster per-capita susceptible replenishment rate by decreasing the susceptible proportion at equilibrium,  $S^*$ . For a simple SIR model that assumes a life-long immunity, we can show analytically that pathogen resilience is proportional to the per-capita rate of susceptible replenishment (Materials and Methods). Overall, these observations suggest that a faster per-capita susceptible replenishment rate causes the system to be more resilient.

By taking the average values of empirical resilience for each pathogen, we were able to map each pathogen onto a set of parameters of the SIRS model that are consistent with corresponding resilience estimates (Figure 5A). Across all pathogens we considered, we estimated that the average duration of immunity is likely to be short ( $< 4$  years) across a plausible range of  $\mathcal{R}_0$  ( $< 6$ ). We were also able to obtain a plausible range of susceptible replenishment rates for each pathogen (Figure 5B), but there was a large uncertainty in the estimates for susceptible replenishment rates due to a lack of one-to-one correspondence between susceptible replenishment rates and pathogen resilience.

342 **Pathogen resilience determines sensitivity to stochastic perturbations**

343

344 Even in the absence of major pandemic perturbations, host-pathogen systems are  
 345 expected to experience continued perturbations of varying degrees from changes in  
 346 epidemiological conditions, such as human behavior, climate, and viral evolution.  
 347 These perturbations can also arise from demographic stochasticity, which is inher-  
 348 ent to any ecological system. Here, we used a seasonally unforced SIRS model with  
 349 constant birth and death rates to explore how resilience of a host-pathogen sys-  
 350 tem determines the sensitivity to perturbations caused by demographic stochasticity  
 351 (Materials and Methods).

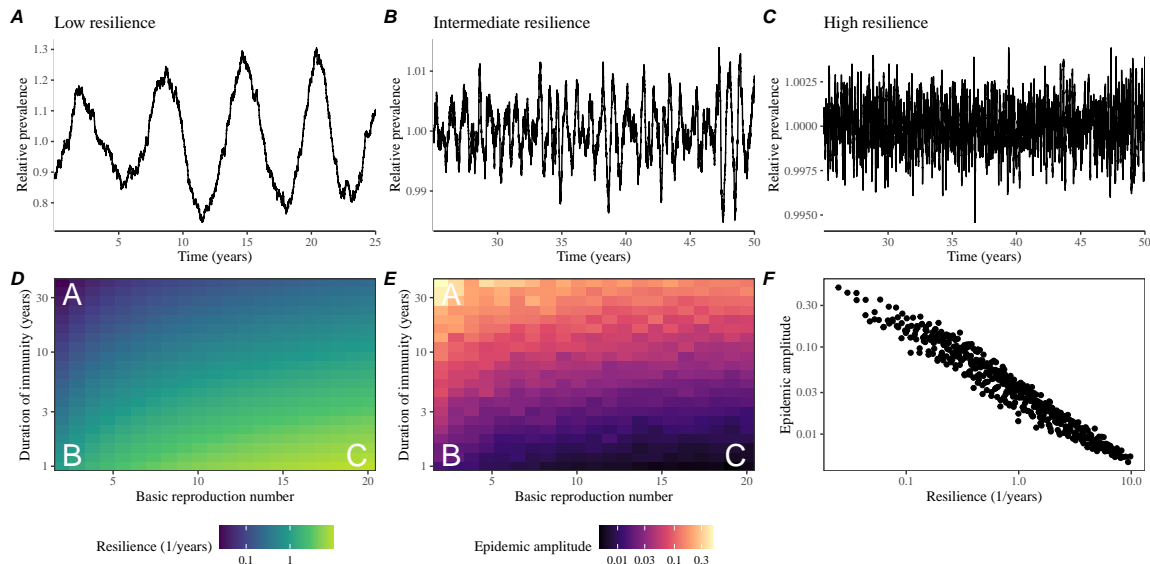


Figure 6: **Linking resilience of a host-pathogen system to its sensitivity to stochastic perturbations.** (A–C) Epidemic trajectories of a stochastic SIRS model across three different resilience values: low, intermediate, and high. The relative prevalence was calculated by dividing infection prevalence by its mean value. (D) Intrinsic resilience of a system as a function of the basic reproduction number  $\mathcal{R}_0$  and the duration of immunity. (E) Epidemic amplitude as a function of the basic reproduction number  $\mathcal{R}_0$  and the duration of immunity. The epidemic amplitude corresponds to  $(\max I - \min I)/(2\bar{I})$ , where  $\bar{I}$  represents the mean prevalence. Labels A–C in panels D and E correspond to scenarios shown in panels A–C. (F) The relationship between pathogen resilience and epidemic amplitude.

352 We found that resilience of a host-pathogen system determines the amount of de-  
 353 viation from the deterministic trajectory caused by demographic stochasticity, with  
 354 less resilient systems experiencing larger deviations (Figure 6). Notably, less resilient  
 355 systems also exhibited slower epidemic cycles (Figure 6A–C). The periodicity of this

356 epidemic cycle matched those predicted by the intrinsic periodicity of the system  
357 (Supplementary Figure S15) where the intrinsic resilience of the system is inversely  
358 proportional to its intrinsic periodicity (Supplementary Figure S16). However, we  
359 note that the interplay between seasonal transmission and intrinsic periodicity can  
360 also lead to complex cycles, as illustrated by a recent analysis of *Mycoplasma pneumoniae*  
361 dynamics [23].

362 We also note that the intrinsic resilience is not the sole determinant for how sen-  
363 sitive the system is to stochastic perturbations. For example, the population size  
364 and average duration of infection also affect the amount of deviation from the deter-  
365 ministic trajectory caused by demographic stochasticity, even though these quantities  
366 have little to no impact on the intrinsic resilience (Supplementary Figure S17). These  
367 conclusions were robust for the seasonally forced SIRS model, where the amount of  
368 deviation from the deterministic trajectory depends on the corresponding resilience  
369 of theseasonally unforced system (Supplementary Figure S18).

## 370 Discussion

371 COVID-19 pandemic interventions caused major disruptions to circulation patterns  
372 of both respiratory and non-respiratory pathogens, adding challenges to predicting  
373 their future dynamics [1, 2, 3, 4]. However, these perturbations offer large-scale natu-  
374 ral experiments for understanding how different pathogens respond to perturbations.  
375 In this study, we showed that pathogen re-emergence patterns following pandemic  
376 perturbations can be characterized through the lens of ecological resilience and pre-  
377 sented a new method for estimating pathogen resilience from time series data. We  
378 showed that variation in pathogen resilience can be explained by the differences in  
379 susceptible host dynamics, where faster replenishment of the susceptible pool corre-  
380 sponds to a more resilient host-pathogen system. Finally, we showed that pathogen  
381 resilience also determines the sensitivity to stochastic perturbations.

382 We analyzed case time series of common respiratory infections and norovirus  
383 infections from Canada, Hong Kong, Korea, and the US to estimate their resilience.  
384 Overall, we estimated the resilience of these pathogens to range from 0.4/year to  
385 1.8/year, which is 3–14 times more resilient than prevaccination measles. Consistent  
386 with other epidemiological evidence [24, 25, 26, 27], these resilience estimates indicate  
387 that common respiratory pathogens and norovirus likely exhibit faster susceptible  
388 replenishment and are therefore more persistent, indicating potential challenges in  
389 controlling these pathogens.

390 Based on our resilience estimates, we made phenomenological predictions about  
391 when each pathogen will return to their endemic cycles. Our main regression analy-  
392 sis was able to accurately distinguish which pathogens should have already returned  
393 before the end of 2024. However, there were two main exceptions (i.e., norovirus in  
394 Hong Kong and rhinovirus/enterovirus in the US), suggesting that these pathogens  
395 may be converging to new endemic cycles or experiencing long-term transient behav-

396 ior. These changes may reflect changes in surveillance or actual shift in the dynamics,  
397 caused by permanent changes in behavior or population-level immunity. While it may  
398 seem unlikely that permanent changes in behavior would only affect a few pathogens  
399 and not others, we cannot rule out this possibility given differences in the observed  
400 mean age of infections and therefore the differences in age groups that primarily drive  
401 transmission [28, 29]. Differences in the mode of transmission between respiratory  
402 vs gastrointestinal pathogens may also contribute to the differences in responses to  
403 pandemic perturbations.

404 For almost half of the pathogens we considered, we predicted that their return  
405 to original epidemic patterns is imminent. However, our evaluation of out-of-sample  
406 predictions suggested major challenges in predicting the exact timing of pathogen  
407 return as well as estimating pathogen resilience from limited data. Therefore, our  
408 estimates of prediction timing should be taken as a ballpark estimate, rather than  
409 precise timing. We will also need a few more years of data to test whether these  
410 pathogens will eventually return to their original dynamics or eventually converge to  
411 a different attractor. We also cannot rule out the possibility that some pathogens may  
412 exhibit long-term transient behaviors following pandemic perturbations. Overall,  
413 these observations echo earlier studies that highlighted the long-lasting impact of  
414 pandemic perturbations [8, 30, 31, 4, 23].

415 We showed that susceptible host dynamics shape pathogen resilience, where faster  
416 replenishment of the susceptible population causes the pathogen to be more resilient.  
417 For simplicity, we focused on waning immunity and birth as the main drivers of the  
418 susceptible host dynamics but other mechanisms can also contribute to the replen-  
419 ishment of the susceptible population. In particular, pathogen evolution, especially  
420 the emergence of antigenically novel strains, can cause effective waning of immunity  
421 in the population; therefore, we hypothesize that the rate of antigenic evolution is  
422 likely a key feature of pathogen resilience. Future studies should explore the relation-  
423 ship between the rate of evolution and resilience for antigenically evolving pathogens.  
424 This result also highlights the importance of detailed measurements of changes in the  
425 susceptible population through immune assays for understanding pathogen dynamics  
426 [32].

427 Quantifying pathogen resilience also offers novel approaches to validating population-  
428 level epidemiological models. So far, most model validation in infectious disease ecol-  
429 ogy is based on the ability of a model to reproduce the observed epidemic dynamics  
430 and to predict future dynamics [33, 34, 26, 35, 36]. However, many models can  
431 perform similarly under these criteria. For example, two major RSV models have  
432 been proposed to explain biennial epidemic patterns: (1) a stage- and age-structured  
433 model that allows disease severity to vary with number of past infections and age of  
434 infection [26] and (2) a pathogen-interaction model that accounts for cross immunity  
435 between RSV and human metapneumovirus [34]. Since both models can accurately  
436 reproduce the observed epidemic patterns, standard criteria for model validation  
437 do not allow us to distinguish between these two models from population-level data  
438 alone. Instead, it would be possible to measure the empirical resilience of each model

439 by simulating various perturbations and comparing the simulations to estimates of  
440 empirical resilience from data, using pandemic perturbations as a reference.

441 There are several limitations to our work. First, we did not extensively explore  
442 other approaches to reconstructing the attractor. Recent studies showed that more  
443 sophisticated approaches, such as using non-uniform embedding, can provide more  
444 robust reconstruction for noisy data [22]. In the context of causal inference, choices  
445 about embedding can have major impact on the resulting inference [37]. Our re-  
446 silience estimates are likely overly confident given a lack of uncertainties in attractor  
447 reconstruction as well as the simplicity of our statistical framework. Nonetheless,  
448 as illustrated in our sensitivity analyses, inferences about pathogen resilience in our  
449 SIRS model appear to be robust to decisions about embedding lags and dimensions—  
450 this is because tracking the rate at which the system approaches the attractor is likely  
451 a much simpler problem than making inferences about causal directionality. Short  
452 pre-pandemic time series also limit our ability to accurately reconstruct the attrac-  
453 tor and contribute to the crudeness of our resilience estimates; although this is less  
454 likely a problem for respiratory pathogens that are strongly annual, our attractor  
455 reconstruction may be inaccurate for those exhibiting multi-annual cycles, such as  
456 adenovirus in Hong Kong and Korea. Our framework also does not allow us to dis-  
457tinguish whether a system has settled to a new attractor or is experiencing long-term  
458 transient behavior. Uncertainties in pathogen dynamics due to changes in testing  
459 patterns further contribute to the crudeness of our resilience estimates.

460 While attractor reconstruction allows us to make model-free inferences of pathogen  
461 resilience, it does not allow us to tease apart how different mechanisms contribute  
462 to the resilience a host-pathogen system. Using the simple SIRS model, we illus-  
463 trated that susceptible host dynamics are key determinants of pathogen resilience,  
464 but we also found that there isn't a one-to-one correspondence between per capita  
465 replenishment rate of the susceptible population and pathogen resilience estimates.  
466 Future studies should explore using mechanistic models to explain heterogeneity in  
467 resilience estimates across different pathogens.

468 Finally, our simulation-based analyses primarily focused on single-strain systems,  
469 but real-world pathogens can interact with other pathogens, which can result in com-  
470plex dynamics [38, 39]. To address this limitation, we considered a simple model of  
471 two competing strains (via cross immunity) and showed that the resilience of a cou-  
472pled system can be measured by studying the dynamics of either strain. However, this  
473 conclusion likely depends on the strength and mechanism of strain interactions. For  
474 example, ecological interference between two unrelated pathogens [38] will likely gen-  
475 erate weaker coupling than cross-immunity between related pathogens; in the former  
476 case, we do not necessarily expect two unrelated pathogens to have same resilience  
477 despite their ecological interference. Some pathogen strains can also exhibit positive  
478 interactions where infection by one strain can lead to an increased transmission of  
479 another competing strain. For example, previous studies showed that an increased  
480 dengue transmission through antibody-dependent enhancement can permit coexis-  
481 tence and persistence of competing strains [40]; since pathogen transmissibility is a

482 major determinant of pathogen resilience, we tentatively hypothesize that positive  
483 interactions such as antibody-dependent enhancement may increase the resilience of  
484 a system. Future studies should explore how different mechanisms of pathogen inter-  
485 actions contribute to the resilience of each competing pathogen as well as the entire  
486 system. Despite these limitations, our study illustrates that quantifying pathogen  
487 resilience can provide novel insights into pathogen dynamics. Furthermore, our qual-  
488 itative prediction that common respiratory pathogens are more resilient than pre-  
489 vaccination measles is also likely to be robust, given how rapidly many respiratory  
490 pathogens returned to their original cycles following pandemic perturbations.

491 Predicting the impact of anthropogenic changes on infectious disease dynamics  
492 is a fundamental aim of infectious disease research in a rapidly changing world. Our  
493 study illustrates that how a host-pathogen system responds to both small and large  
494 perturbations is largely predictable through the lens of ecological resilience. In par-  
495 ticular, quantifying the resilience of a host-pathogen system offers a unique insight  
496 into questions about endemic pathogens' responses to pandemic perturbations, in-  
497 cluding whether some pathogens will exhibit long-lasting impact from the pandemic  
498 perturbation or not. More broadly, a detailed understanding of the determinants of  
499 pathogen resilience can provide deeper understanding of pathogen persistence.

## 500 Materials and Methods

### 501 Data

502 We gathered time series on respiratory infections from Canada, Hong Kong, Korea,  
503 and United States (US). As a reference, we also included time series data on norovirus  
504 infections when available. In contrast to respiratory pathogens, we hypothesized  
505 gastrointestinal viruses, such as norovirus, to be differently affected by pandemic  
506 perturbations.

507 Weekly time series of respiratory infection cases in Canada came from a publicly  
508 available website by the Respiratory Virus Detection Surveillance System, which  
509 collects data from select laboratories across Canada [41]. Weekly time series of  
510 respiratory infection cases in Hong Kong came from a publicly available website  
511 by the Centre for Health Protection, Department of Health [42, 43]. Weekly time  
512 series of acute respiratory infection cases in Korea came from a publicly available  
513 website by the Korea Disease Control and Prevention Agency [44]. Finally, weekly  
514 time series of respiratory infection cases in the US were obtained from the National  
515 Respiratory and Enteric Virus Surveillance System (NREVSS). Readers can request  
516 the data from NREVSS at [nrevss@cdc.gov](mailto:nrevss@cdc.gov). Time series on number of tests were also  
517 available in Canada, Hong Kong, and the US, but not in Korea.

518 **Data processing**

519 For all time series, we rounded every year to 52 weeks by taking the average number  
520 of cases and tests between the 52nd and 53rd week. We also rescaled all time series to  
521 account for changes in testing patterns, which were then used for the actual analysis.

522 For Canada, an increase in testing was observed from 2013 to 2024 (Supplementary  
523 Figure S17). To account for this increase, we calculated a 2 year moving average  
524 for the number of tests for each pathogen, which we used as a proxy for testing effort.  
525 Then, we divided the smoothed testing patterns by the smoothed value at the final  
526 week such that the testing effort has a maximum of 1. We then divided weekly cases  
527 by the testing effort to obtain a scaled case time series. A similar approach was used  
528 earlier for an analysis of RSV time series in the US to account for changes in testing  
529 patterns [26].

530 For Hong Kong, we applied the same scaling procedure to the time series as we  
531 did for Canada. In this case, we only adjusted for testing efforts up to the end of 2019  
532 because there was a major reduction in testing for common respiratory pathogens  
533 between 2020 and 2023 (Supplementary Figure S18).

534 For Korea, while we did not have information on testing, the reported number  
535 of respiratory infections consistently increased from 2013 to the end of 2019, which  
536 we interpreted as changes in testing patterns (Supplementary Figure S19). Since  
537 we did not have testing numbers, we used the weekly sum of all acute respiratory  
538 viral infection cases as a proxy for testing, which were further smoothed with moving  
539 average and scaled to have a maximum of 1. For Korea, we also only adjusted for  
540 testing efforts up to the end of 2019.

541 In the US, there has been a large increase in testing for some respiratory pathogens,  
542 especially RSV, which could not be corrected by simple scaling (Supplementary Figure  
543 S20). Instead, we derived an incidence proxy by multiplying the test positivity  
544 with influenza-like illness positivity, which was taken from [https://gis.cdc.gov/  
545 grasp/fluvie](https://gis.cdc.gov/grasp/fluvie). This method of estimating an incidence proxy has been recently applied in the analysis of seasonal coronaviruses [7]  
546 and *Mycoplasma pneumoniae* infections [4]. Detailed assumptions and justifications  
547 are provided in [45].

549 **Data summary**

550 To make qualitative comparisons between pre- and post-perturbation dynamics of  
551 respiratory pathogen circulation patterns, we calculated the mean seasonal patterns  
552 using time series of either rescaled cases or incidence proxy estimates before 2020. We  
553 did so by taking the mean value in each week across all years before 2020. Confidence  
554 intervals around the means were calculated using a simple t test.

555 **Estimating pathogen resilience**

556 In order to measure pathogen resilience from surveillance data, we first reconstructed  
 557 the empirical pre-pandemic attractor of the system using Takens' embedding theorem  
 558 [17]. Specifically, for a given pathogen, we took the pre-pandemic (before 2020) case  
 559 time series  $C(t)$  and reconstructed the attractor using delayed embedding with a  
 560 uniform delay of  $\tau$  and dimension  $M$ :

$$X_{\tau,m}(t) = \langle \log(C(t) + 1), \log(C(t - \tau) + 1), \dots, \log(C(t - (M - 1)\tau) + 1) \rangle. \quad (2)$$

561 Here, the delay  $\tau$  was determined by calculating the autocorrelation of the logged  
 562 pre-pandemic time series and asking when the autocorrelation crosses 0 for the first  
 563 time [22]; a typical delay for an annual outbreak is around 13 weeks.

564 Then, for a given delay  $\tau$ , we determined the embedding dimension  $M$  using the  
 565 false nearest neighbors approach [21, 22]. To do so, we started with an embedding  
 566 dimension  $e$  and constructed a set of points  $A_{\tau,e} = \{X_{\tau,e}(t) | t < 2020\}$ . Then, for  
 567 each point  $X_{\tau,e}(t)$ , we determined the nearest neighbor from the set  $A_{\tau,e}$ , which we  
 568 denote  $X_{\tau,e}(t_{nn})$  for  $t \neq t_{nn}$ . Then, if the distance between these two points in the  
 569  $e+1$  dimension,  $D_{\tau,e+1}(t) = \|X_{\tau,e+1}(t_{nn}) - X_{\tau,e+1}(t)\|_2$ , is larger than their distance in  
 570 the  $e$  dimension,  $D_{\tau,e}(t) = \|X_{\tau,e}(t_{nn}) - X_{\tau,e}(t)\|_2$ , these two points are deemed to be  
 571 false nearest neighbors; specifically, we used a threshold  $R$  for the ratio between two  
 572 distances  $D_{\tau,e+1}(t)/D_{\tau,e}(t)$  to determine false nearest neighbors. The first embed-  
 573 ding dimension  $e$  that does not have any false nearest neighbors corresponds to the  
 574 embedding dimension  $M$  for a given pathogen-country pair. For the main analysis,  
 575 we used  $R = 10$ , which was chosen from a sensitivity analysis against simulated data  
 576 (Supplementary Text). Once we determined the embedding lag  $\tau$  and dimension  $M$ ,  
 577 we apply the embedding to the entire time series and calculate the nearest neigh-  
 578 bor distance against the attractor  $A_{\tau,M}$  to obtain a time series of distance from the  
 579 attractor  $D_{\tau,M}(t)$ .

580 From a time series of distances from the attractor, we estimated pathogen re-  
 581 silience by fitting a linear regression to an appropriate window. To automatically  
 582 select fitting windows, we began by smoothing the distance time series using locally  
 583 estimated scatterplot smoothing (LOESS) to obtain  $\hat{D}_{\tau,M}(t)$ , where the smoothing  
 584 is performed on a log scale and exponentiated afterwards. This smoothing allowed  
 585 us to find appropriate threshold values for selecting fitting windows that are insensi-  
 586 tive to errors in our estimates of distance from the attractor. Then, we determined  
 587 threshold values ( $T_{\text{start}}$  and  $T_{\text{end}}$ ) for the smoothed distances and choose the fitting  
 588 window based on when  $\hat{D}_{\tau,M}(t)$  crosses these threshold values for the first time.  
 589 These thresholds were determined by first calculating the maximum distance,

$$\max \hat{D} = \max \hat{D}_{\tau,M}(t), \quad (3)$$

590 and the mean pre-pandemic distance,

$$\hat{D}_{\text{mean}} = \frac{1}{N_{t < 2020}} \sum_{t < 2020} \hat{D}_{\tau,M}(t), \quad (4)$$

591 as a reference, and then dividing their ratios into  $K$  equal bins,

$$T_{\text{start}} = \hat{D}_{\text{mean}} \times \left( \frac{\max \hat{D}}{\hat{D}_{\text{mean}}} \right)^{(K-a)/K}, \quad (5)$$

$$T_{\text{end}} = \hat{D}_{\text{mean}} \times \left( \frac{\max \hat{D}}{\hat{D}_{\text{mean}}} \right)^{a/K}, \quad (6)$$

592 where  $a$  represents the truncation threshold. This allows us to discard the initial  
 593 period during which the distance increases (from the introduction of intervention  
 594 measures) and the final period during which the distance plateaus (as the system  
 595 reaches an attractor). The fitting window is determined based on when the smoothed  
 596 distance  $\hat{D}_{\tau,M}(t)$  crosses these threshold values for the first time; then, we fit a  
 597 linear regression to logged (unsmoothed) distances  $\log D_{\tau,M}(t)$  using that window.  
 598 Alongside the threshold  $R$  for the false nearest neighbors approach, we tested optimal  
 599 choices for  $K$  and  $a$  values using simulations (Supplementary Text). We used  $K = 19$   
 600 and  $a = 2$  throughout the paper based on the simulation results. We excluded data  
 601 sets from the regression analysis if the logged average of the estimated distance from  
 602 the attractor during the last year is at least 2 fold greater than the logged average  
 603 of the pre-pandemic distance from the attractor.

604 To evaluate the ability to predict precise timing of return time for out-of-sample  
 605 observations, we applied the same framework using data up to the 26th week of  
 606 2023. In doing so, we compared the predicted return time with the observed return  
 607 time, which was determined based on when the estimated distance from the attractor  
 608 became close enough to pre-pandemic levels, using  $1.2\hat{D}_{\text{mean}}$  as our threshold. We  
 609 note that this approach necessarily underestimates the observed return time and  
 610 therefore should be interpreted as a conservative estimate.

## 611 Mathematical modeling

612 Throughout the paper, we use a series of mathematical models to illustrate the  
 613 concept of pathogen resilience and to understand the determinants of pathogen re-  
 614 silience. In general, the intrinsic resilience of a given system is given by the largest  
 615 real part of the eigenvalues of the linearized system at endemic equilibrium. Here, we  
 616 focus on the SIRS model with demography (birth and death) and present the details  
 617 of other models in Supplementary Text. The SIRS (Susceptible-Infected-Recovered-  
 618 Susceptible) model is the simplest model that allows for waning of immunity, where  
 619 recovered (immune) individuals are assumed to become fully susceptible after an  
 620 average of  $1/\delta$  time period. The dynamics of the SIRS model is described by the  
 621 following set of differential equations:

$$\frac{dS}{dt} = \mu - \beta(t)SI - \mu S + \delta R \quad (7)$$

$$\frac{dI}{dt} = \beta(t)SI - (\gamma + \mu)I \quad (8)$$

$$\frac{dR}{dt} = \gamma I - (\delta + \mu)R \quad (9)$$

622 where  $\mu$  represents the birth and death rates,  $\beta(t)$  represents the time-varying trans-  
 623 mission rate, and  $\gamma$  represents the recovery rate. The basic reproduction number  
 624  $\mathcal{R}_0(t) = \beta(t)/(\gamma + \mu)$  is defined as the average number of secondary infections that  
 625 a single infected individual would cause in a fully susceptible population at time  $t$   
 626 and measures the intrinsic transmissibility of a pathogen.

627 When we introduced the idea of pathogen resilience (Figure 2), we imposed sinu-  
 628 soidal changes to the transmission rate to account for seasonal transmission,

$$\beta(t) = b_1(1 + \theta \cos(2\pi(t - \phi)))\alpha(t), \quad (10)$$

629 where  $b_1$  represents the baseline transmission rate,  $\theta$  represents the seasonal ampli-  
 630 tude, and  $\phi$  represents the seasonal offset term. Here, we also introduced an extra  
 631 multiplicative term  $\alpha(t)$  to account for the impact of pandemic perturbations, where  
 632  $\alpha(t) < 1$  indicates transmission reduction. Figure 2A and 2B were generated assum-  
 633 ing  $b_1 = 3 \times (365/7 + 1/50)/\text{years}$ ,  $\theta = 0.2$ ,  $\phi = 0$ ,  $\mu = 1/50/\text{years}$ ,  $\gamma = 365/7/\text{years}$ ,  
 634 and  $\delta = 1/2/\text{years}$ . Specifically,  $b_1 = 3 \times (365/7 + 1/50)/\text{years}$  implies  $\mathcal{R}_0 = 3$ , where  
 635  $(365/7 + 1/50)/\text{years}$  represent the rate of recovery. In Figure 2A, we imposed a 50%  
 636 transmission reduction for 6 months from 2020:

$$\alpha(t) = \begin{cases} 0.5 & 2020 \leq t < 2020.5 \\ 1 & \text{otherwise} \end{cases} \quad (11)$$

637 In Figure 2B, we imposed a 50% transmission reduction for 6 months from 2020 and  
 638 a permanent 10% reduction onward:

$$\alpha(t) = \begin{cases} 1 & t < 2020 \\ 0.5 & 2020 \leq t < 2020.5 \\ 0.9 & 2020.5 \leq t \end{cases} \quad (12)$$

639 In both scenarios, we simulated the SIRS model from the same initial conditions  
 640 ( $S(0) = 1/\mathcal{R}_0$ ,  $I(0) = 1 \times 10^{-6}$ , and  $R(0) = 1 - S(0) - I(0)$ ) from 1900 until 2030.  
 641 Throughout the paper, all deterministic models were solved using the **lsoda** solver  
 642 from the **deSolve** package [46] in R [47].

643 To measure the empirical resilience of the SIRS model (Figure 2C and 2F), we  
 644 computed the normalized distance between post-intervention susceptible and logged  
 645 infected proportions and their corresponding unperturbed values at the same time:

$$\sqrt{\left(\frac{S(t) - S_{\text{unperturbed}}(t)}{\sigma_S}\right)^2 + \left(\frac{\log I(t) - \log I_{\text{unperturbed}}(t)}{\sigma_{\log I}}\right)^2}, \quad (13)$$

646 where  $\sigma_S$  and  $\sigma_{\log I}$  represent the standard deviation in the unperturbed susceptible  
 647 and logged infected proportions. The unperturbed values were obtained by simulat-  
 648 ing the same SIRS model without pandemic perturbations ( $\alpha = 1$ ). We normalized

the differences in susceptible and logged infected proportions to allow both quantities to equally contribute to the changes in distance from the attractor. We used logged prevalence, instead of absolute prevalence, in order to capture epidemic dynamics in deep troughs during the intervention period. In Supplementary Materials, we also compared how the degree of seasonal transmission affects empirical resilience by varying  $\theta$  from 0 to 0.4; when we assumed no seasonality ( $\theta = 0$ ), we did not normalize the distance because the standard deviation of pre-intervention dynamics are zero.

We used the SIRS model to understand how underlying epidemiological parameters affect pathogen resilience and determine the relationship to underlying susceptible host dynamics. For the simple SIRS model without seasonal transmission ( $\theta = 0$ ), the intrinsic resilience equals

$$-\frac{\text{Re}(\lambda)}{2} = \frac{\delta + \beta I^* + \mu}{2}. \quad (14)$$

Here,  $I^*$  represents the prevalence at endemic equilibrium:

$$I^* = \frac{(\delta + \mu)(\beta - (\gamma + \mu))}{\beta(\delta + \gamma + \mu)}. \quad (15)$$

The susceptible replenishment rate is given by

$$S_{\text{replenish}} = \frac{\mu + \delta R}{S^*}, \quad (16)$$

where  $S^* = 1/\mathcal{R}_0$  represents the equilibrium proportion of susceptible individuals. We varied the basic reproduction number  $\mathcal{R}_0$  between 1.1 to 6 and the average duration of immunity  $1/\delta$  between 2 to 4 years, and computed these two quantities. In doing so, we fixed all other parameters:  $\mu = 1/80/\text{years}$  and  $\gamma = 365/7/\text{years}$ . When infection provides a life-long immunity ( $\delta = 0$ ), the intrinsic resilience is inversely proportional to the susceptible replenishment rate:

$$-\frac{\text{Re}(\lambda)}{2} = \frac{\mu}{2S^*} = \frac{S_{\text{replenish}}}{2}. \quad (17)$$

Finally, we used a seasonally unforced stochastic SIRS model without demography to understand how pathogen resilience affects sensitivity of the system to demographic stochasticity (see Supplementary Text for the details of the stochastic SIRS model). By varying the basic reproduction number  $\mathcal{R}_0$  between 2 to 20 and the average duration of immunity  $1/\delta$  between 1 to 40 years, we ran the SIRS model for 100 years and computed the epidemic amplitude, which we defined as  $(\max I - \min I)/(2\bar{I})$ . Each simulation began from the equilibrium, and we truncated the initial 25 years before computing the epidemic amplitude. In doing so, we assumed  $\gamma = 365/7/\text{years}$  and fixed the population size to 1 billion to prevent any fadeouts. We also considered a seasonally forced stochastic SIRS model without demography, assuming an amplitude of seasonal forcing of 0.04; in this case, we computed the relative epidemic amplitude by comparing the deterministic and stochastic trajectories (Supplementary Materials).

682 **Acknowledgement**

683 We thank Anthony R. Ives for helpful discussion. We thank Centers for Disease  
684 Control and Prevention, National Respiratory and Enteric Virus Surveillance System  
685 (NREVSS) for providing time series data for respiratory infection cases in the US.

686 **Data availability**

687 All data and code are stored in a publicly available GitHub repository (<https://github.com/cobeylab/return-time>).  
688

689 **Funding**

690 S.W.P. is a Peter and Carmen Lucia Buck Foundation Awardee of the Life Sciences  
691 Research Foundation. B.F.N. acknowledges financial support from the Carlsberg  
692 Foundation (grant no. CF23-0173). B.T.G is supported by Princeton Catalysis Initiative  
693 and Princeton Precision Health. S.C. is supported by Federal funds from the  
694 National Institute of Allergy and Infectious Diseases, National Institutes of Health,  
695 Department of Health and Human Services under CEIRR contract 75N93021C00015.  
696 The content is solely the responsibility of the authors and does not necessarily repre-  
697 sent the official views of the NIAID or the National Institutes of Health. This project  
698 has been funded in whole or in part with Federal funds from the National Cancer In-  
699 stitute, National Institutes of Health, under Prime Contract No. 75N91019D00024,  
700 Task Order No. 75N91023F00016 (B.F.N., E.H., and B.T.G). The content of this  
701 publication does not necessarily reflect the views or policies of the Department of  
702 Health and Human Services, nor does mention of trade names, commercial products  
703 or organizations imply endorsement by the U.S. Government.

704 **Supplementary Text**

705 **Resilience of a stage-structured system.**

706 In Figure 2G–I, we used a more realistic, stage-structured model to illustrate how  
 707 transient phenomena can cause the system to slow down. Specifically, we used the  
 708 stage-structured RSV model proposed by [26], which assumes that subsequent rein-  
 709 fections cause an individual to become less susceptible and transmissible than previ-  
 710 ous infections. In contrast to a standard SIRS model, this model does not include a  
 711 recovered compartment, which allow for temporary protection against new infections,  
 712 and assumes that recovered individuals are immediately susceptible to new infections.  
 713 The model dynamics can be described as follows:

$$\frac{dM}{dt} = \mu - (\omega + \mu)M \quad (S1)$$

$$\frac{dS_0}{dt} = \omega M - (\lambda(t) + \mu)S_0 \quad (S2)$$

$$\frac{dI_1}{dt} = \lambda(t)S_0 - (\gamma_1 + \mu)I_1 \quad (S3)$$

$$\frac{dS_1}{dt} = \gamma_1 I_1 - (\sigma_1 \lambda(t) + \mu)S_1 \quad (S4)$$

$$\frac{dI_2}{dt} = \sigma_1 \lambda(t)S_1 - (\gamma_2 + \mu)I_2 \quad (S5)$$

$$\frac{dS_2}{dt} = \gamma_2 I_2 - (\sigma_2 \lambda(t) + \mu)S_2 \quad (S6)$$

$$\frac{dI_3}{dt} = \sigma_2 \lambda(t)S_2 - (\gamma_3 + \mu)I_3 \quad (S7)$$

$$\frac{dS_3}{dt} = \gamma_3 I_3 - (\sigma_3 \lambda(t) + \mu)S_3 + \gamma_4 I_4 \quad (S8)$$

$$\frac{dI_4}{dt} = \sigma_3 \lambda(t)S_3 - (\gamma_4 + \mu)I_4 \quad (S9)$$

714 where  $M$  represents the proportion of individuals who are maternally immune;  $S_i$   
 715 represents the proportion of individuals who are susceptible after  $i$  prior infections;  $I_i$   
 716 represents the proportion of individuals who are currently (re)-infected with their  $i$ -th  
 717 infection;  $\mu$  represents the birth and death rates;  $1/\omega$  represents the mean duration  
 718 of maternal immunity;  $1/\gamma_i$  represents the mean duration of infection;  $\lambda(t)$  represents  
 719 the force of infection; and  $\sigma_i$  represents the reduction in susceptibility for the  $i$ -th  
 720 reinfection. The force of infection is modeled using a sinusoidal function:

$$\beta(t) = b_1(1 + \theta \cos(2\pi(t - \phi)))\alpha(t) \quad (S10)$$

$$\lambda(t) = \beta(I_1 + \rho_1 I_2 + \rho_2(I_3 + I_4)), \quad (S11)$$

721 where  $b_1$  represents the baseline transmission rate;  $\theta$  represents the seasonal ampli-  
 722 tude;  $\phi$  represents the seasonal offset term;  $\alpha(t)$  represents the intervention effect;

723 and  $\rho_i$  represents the impact of immunity on transmission reduction. We used the  
 724 following parameters to simulate the impact of interventions on epidemic dynam-  
 725 ics [26]:  $b_1 = 9 \times (365/10 + 1/80)/\text{years}$ ,  $\theta = 0.2$ ,  $\phi = -0.1$ ,  $\omega = 365/112/\text{years}$ ,  
 726  $\gamma_1 = 365/10/\text{years}$ ,  $\gamma_2 = 365/7/\text{years}$ ,  $\gamma_3 = 365/5/\text{years}$ ,  $\sigma_1 = 0.76$ ,  $\sigma_2 = 0.6$ ,  
 727  $\sigma_3 = 0.4$ ,  $\rho_1 = 0.75$ ,  $\rho_2 = 0.51$ , and  $\mu = 1/80/\text{years}$ . We assumed a 50% transmis-  
 728 sion reduction for 6 months from 2020:

$$\alpha(t) = \begin{cases} 0.5 & 2020 \leq t < 2020.5 \\ 1 & \text{otherwise} \end{cases} \quad (\text{S12})$$

729 The model was simulated from 1900 to 2030 using the following initial conditions:  
 730  $M = 0$ ,  $S_0 = 1/\mathcal{R}_0 - I_1$ ,  $I_1 = 1 \times 10^{-6}$ ,  $S_1 = 1 - 1/\mathcal{R}_0$ ,  $I_2 = 0$ ,  $S_2 = 0$ ,  $I_3 = 0$ ,  
 731  $S_3 = 0$ , and  $I_4 = 0$ . For the phase plane analysis (Figure 2H) and distance analysis  
 732 (Figure 2I), we relied on the average susceptibility,

$$\bar{S} = S_0 + \sigma_1 S_1 + \sigma_2 S_2 + \sigma_3 S_3, \quad (\text{S13})$$

733 and total prevalence,

$$I_{\text{total}} = I_1 + I_2 + I_3 + I_4. \quad (\text{S14})$$

734 These quantities were used to compute the normalized distance from the attractor,  
 735 as described in the main text.

736 We note that this system, without seasonally forced transmission rates, has 9  
 737 eigenvalues: -73.01, -53.11, -38.90, -3.27,  $-0.82+2.57i$ ,  $-0.82-2.57i$ , -1.61, -1.18, and  
 738 -0.01 (in the unit of 1/years). While the eigenvalue -0.01 has the largest real part,  
 739 the magnitude is too close to 0 for the impact of this eigenvalue to be reflected in  
 740 our resilience estimates. Instead, we chose real parts of the eigenvalues  $-0.82 \pm 2.57i$   
 741 as our intrinsic resilience for this system and plotted them in Figure 2I; as we can  
 742 see in this figure, this value captures the return rate of the system to the attractor.

## 743 Resilience of a multistrain system.

744 We used a simple two-strain model to show that a multistrain host-pathogen system  
 745 that is coupled through cross immunity can be described by a single resilience value.  
 746 The model dynamics can be described as follows [34]:

$$\frac{dS}{dt} = \mu - \mu S - (\lambda_1 + \lambda_2)S + \delta_1 R_1 + \delta_2 R_2 \quad (\text{S15})$$

$$\frac{dI_1}{dt} = \lambda_1 S - (\gamma_1 + \mu)I_1 \quad (\text{S16})$$

$$\frac{dI_2}{dt} = \lambda_2 S - (\gamma_2 + \mu)I_2 \quad (\text{S17})$$

$$\frac{dR_1}{dt} = \gamma_1 I_1 - \lambda_2 \epsilon_{21} R_1 - \delta_1 R_1 + \delta_2 R - \mu R_1 \quad (\text{S18})$$

$$\frac{dR_2}{dt} = \gamma_2 I_2 - \lambda_1 \epsilon_{12} R_2 - \delta_2 R_2 + \delta_1 R - \mu R_2 \quad (\text{S19})$$

$$\frac{dJ_1}{dt} = \lambda_1 \epsilon_{12} R_2 - (\gamma_1 + \mu) J_1 \quad (S20)$$

$$\frac{dJ_2}{dt} = \lambda_2 \epsilon_{21} R_1 - (\gamma_2 + \mu) J_2 \quad (S21)$$

$$\frac{dR}{dt} = \gamma_1 J_1 + \gamma_2 J_2 - \delta_1 R - \delta_2 R - \mu R \quad (S22)$$

where  $S$  represents the proportion of individuals who are fully susceptible to infections by both strains;  $I_1$  represents the proportion of individuals who are infected with strain 1 without prior immunity;  $I_2$  represents the proportion of individuals who are infected with strain 2 without prior immunity;  $R_1$  represents the proportion of individuals who are fully immune against strain 1 and partially susceptible to reinfection by strain 2;  $R_2$  represents the proportion of individuals who are fully immune against strain 2 and partially susceptible to reinfection by strain 1;  $J_1$  represents the proportion of individuals who are infected with strain 1 with prior immunity against strain 2;  $J_2$  represents the proportion of individuals who are infected with strain 2 with prior immunity against strain 1;  $R$  represents the proportion of individuals who are immune to infections from both strains;  $\mu$  represents the birth/death rate;  $\lambda_1$  and  $\lambda_2$  represent the force of infection from strains 1 and 2, respectively;  $\delta_1$  and  $\delta_2$  represent the waning immunity rate;  $\gamma_1$  and  $\gamma_2$  represent the recovery rate;  $\epsilon_{21}$  and  $\epsilon_{12}$  represent the susceptibility to reinfection with strains 2 and 1, respectively, given prior immunity from infection with strains 1 and 2, respectively. The force of infection is modeled as follows:

$$\beta_1 = b_1(1 + \theta_1 \sin(2\pi(t - \phi_1)))\alpha(t) \quad (S23)$$

$$\beta_2 = b_2(1 + \theta_2 \sin(2\pi(t - \phi_2)))\alpha(t) \quad (S24)$$

$$\lambda_1 = \beta_1(I_1 + J_1) \quad (S25)$$

$$\lambda_2 = \beta_2(I_2 + J_2) \quad (S26)$$

In Supplementary Figures S2–S4, we assumed the following parameters:  $b_1 = 2 \times 52/\text{years}$ ,  $b_2 = 4 \times 52/\text{years}$ ,  $\phi_1 = \phi_2 = 0$ ,  $\epsilon_{12} = 0.9$ ,  $\epsilon_{21} = 0.5$ ,  $\gamma_1 = \gamma_2 = 52/\text{years}$ ,  $\delta_1 = \delta_2 = 1/\text{years}$ , and  $\mu = 1/70/\text{years}$ . For all simulations, we assumed a 50% transmission reduction for 6 months from 2020:

$$\alpha(t) = \begin{cases} 0.5 & 2020 \leq t < 2020.5 \\ 1 & \text{otherwise} \end{cases} \quad (S27)$$

The seasonal amplitude  $\theta$  is varied from 0 to 0.4. All simulations were run from 1900 to 2030 with following initial conditions:  $S(0) = 1 - 2 \times 10^{-6}$ ,  $I_1(0) = 1 \times 10^{-6}$ ,  $I_2(0) = 1 \times 10^{-6}$ ,  $R_1(0) = 0$ ,  $R_2(0) = 0$ ,  $J_1(0) = 0$ ,  $J_2(0) = 0$ , and  $R(0) = 0$ .

We considered three scenarios for measuring pathogen resilience: (1) we only have information about strain 1, (2) we only have information about strain 2, and (3) we are unable to distinguish between strains. In the first two scenarios (see panels A–C for strain 1 and panels D–F for strain 2), we considered the dynamics of average

<sup>774</sup> susceptibility for each strain and total prevalence:

$$\bar{S}_1 = S + \epsilon_{12}R_2 \quad (\text{S28})$$

$$\hat{I}_1 = I_1 + J_1 \quad (\text{S29})$$

$$\bar{S}_2 = S + \epsilon_{21}R_1 \quad (\text{S30})$$

$$\hat{I}_2 = I_2 + J_2 \quad (\text{S31})$$

<sup>775</sup> In the third scenario (panels G–I), we considered the dynamics of total susceptible  
<sup>776</sup> and infected populations:

$$\hat{S} = S + R_2 + R_1 \quad (\text{S32})$$

$$\hat{I} = I_1 + J_1 + I_2 + J_2 \quad (\text{S33})$$

<sup>777</sup> These quantities were used to compute the normalized distance from the attractor,  
<sup>778</sup> as described in the main text.

## <sup>779</sup> Estimating intrinsic resilience using a mechanistic model

<sup>780</sup> We tested whether we can reliably estimate the intrinsic resilience of a system by fit-  
<sup>781</sup> ting a mechanistic model. Specifically, we simulated case time series from stochastic  
<sup>782</sup> SIRS and two-strain models and fitted a simple, deterministic SIRS model using a  
<sup>783</sup> Bayesian framework [4, 23, 48].

<sup>784</sup> We simulated the models in discrete time with a daily time step ( $\Delta t = 1$ ),  
<sup>785</sup> incorporating demographic stochasticity:

$$\beta(t) = \mathcal{R}_0 \left( 1 + \theta \cos \left( \frac{2\pi t}{364} \right) \right) \alpha(t)(1 - \exp(-\gamma)) \quad (\text{S34})$$

$$\text{FOI}(t) = \beta(t)I(t - \Delta t)/N \quad (\text{S35})$$

$$B(t) \sim \text{Poisson}(\mu N) \quad (\text{S36})$$

$$\Delta S(t) \sim \text{Binom}(S(t - \Delta t), 1 - \exp(-(\text{FOI}(t) + \mu)\Delta t)) \quad (\text{S37})$$

$$N_{SI}(t) \sim \text{Binom}\left(\Delta S(t), \frac{\text{FOI}(t)}{\text{FOI}(t) + \mu}\right) \quad (\text{S38})$$

$$\Delta I(t) \sim \text{Binom}(I(t - \Delta t), 1 - \exp(-(\gamma + \mu)\Delta t)) \quad (\text{S39})$$

$$N_{IR}(t) \sim \text{Binom}\left(\Delta I(t), \frac{\gamma}{\gamma + \mu}\right) \quad (\text{S40})$$

$$\Delta R(t) \sim \text{Binom}(R(t - \Delta t), 1 - \exp(-(\delta + \mu)\Delta t)) \quad (\text{S41})$$

$$N_{RS}(t) \sim \text{Binom}\left(\Delta R(t), \frac{\delta}{\delta + \mu}\right) \quad (\text{S42})$$

$$S(t) = S(t - \Delta t) + N_{RS}(t) + B(t) - \Delta S(t) \quad (\text{S43})$$

$$I(t) = I(t - \Delta t) + N_{SI}(t) - \Delta I(t) \quad (\text{S44})$$

$$R(t) = R(t - \Delta t) + N_{IR}(t) - \Delta R(t) \quad (\text{S45})$$

where FOI represents the force of infection;  $N_{ij}$  represents the number of individuals moving from compartment  $i$  to  $j$  on a given day; and  $B(t)$  represents the number of new births. All other parameters definitions can be found in the description of the deterministic version of the model. We simulated the model on a daily scale—assuming 364 days in a year so that it can be evenly grouped into 52 weeks—with the following parameters:  $\mathcal{R}_0 = 3$ ,  $\theta = 0.1$ ,  $\gamma = 1/7/\text{days}$ ,  $\delta = 1/(364 \times 2)/\text{days}$ ,  $\mu = 1/(364 \times 50)/\text{days}$ , and  $N = 1 \times 10^8$ . The model was simulated from 1900 to 2030 assuming  $S(0) = N/3$ ,  $I(0) = 100$ , and  $R(0) = N - S(0) - I(0)$ . The observed incidence from the model was then simulated as follows:

$$C(t) = \text{Beta-Binom}(N_{SI}(t), \rho, k), \quad (\text{S46})$$

where  $\rho$  represents the reporting probability and  $k$  represents the overdispersion parameter of beta-binomial distribution. Here, we used the beta-binomial distribution to account for overdispersion in reporting. We assumed  $\rho = 0.002$  (i.e., 0.2% probability) and  $k = 1000$ .

We used an analogous approach for the two-strain model:

$$\beta_1(t) = b_1 \left( 1 + \theta_1 \cos \left( \frac{2\pi(t - \phi_1)}{364} \right) \right) \alpha(t) \quad (\text{S47})$$

$$\beta_2(t) = b_2 \left( 1 + \theta_2 \cos \left( \frac{2\pi(t - \phi_2)}{364} \right) \right) \alpha(t) \quad (\text{S48})$$

$$\text{FOI}_1(t) = \beta_1(t)(I_1(t - \Delta t) + J_1(t - \Delta t))/N \quad (\text{S49})$$

$$\text{FOI}_2(t) = \beta_2(t)(I_2(t - \Delta t) + J_2(t - \Delta t))/N \quad (\text{S50})$$

$$B(t) \sim \text{Poisson}(\mu N) \quad (\text{S51})$$

$$\Delta S(t) \sim \text{Binom}(S(t - \Delta t), 1 - \exp(-(\text{FOI}_1(t) + \text{FOI}_2(t) + \mu)\Delta t)) \quad (\text{S52})$$

$$N_{SI_1}(t) \sim \text{Binom}\left(\Delta S(t), \frac{\text{FOI}_1(t)}{\text{FOI}_1(t) + \text{FOI}_2(t) + \mu}\right) \quad (\text{S53})$$

$$N_{SI_2}(t) \sim \text{Binom}\left(\Delta S(t), \frac{\text{FOI}_2(t)}{\text{FOI}_1(t) + \text{FOI}_2(t) + \mu}\right) \quad (\text{S54})$$

$$\Delta I_1(t) \sim \text{Binom}(I_1(t - \Delta t), 1 - \exp(-(\gamma_1 + \mu)\Delta t)) \quad (\text{S55})$$

$$N_{I_1 R_1}(t) \sim \text{Binom}\left(\Delta I_1(t), \frac{\gamma_1}{\gamma_1 + \mu}\right) \quad (\text{S56})$$

$$\Delta I_2(t) \sim \text{Binom}(I_2(t - \Delta t), 1 - \exp(-(\gamma_2 + \mu)\Delta t)) \quad (\text{S57})$$

$$N_{I_2 R_2}(t) \sim \text{Binom}\left(\Delta I_2(t), \frac{\gamma_2}{\gamma_2 + \mu}\right) \quad (\text{S58})$$

$$\Delta R_1(t) \sim \text{Binom}(R_1(t - \Delta t), 1 - \exp(-(\epsilon_{21}\text{FOI}_2(t) + \rho_1 + \mu)\Delta t)) \quad (\text{S59})$$

$$N_{R_1 S}(t) \sim \text{Binom}\left(\Delta R_1(t), \frac{\rho_1}{\epsilon_{21}\text{FOI}_2(t) + \rho_1 + \mu}\right) \quad (\text{S60})$$

$$N_{R_1 J_2}(t) \sim \text{Binom}\left(\Delta R_1(t), \frac{\epsilon_{21}\text{FOI}_2(t)}{\epsilon_{21}\text{FOI}_2(t) + \rho_1 + \mu}\right) \quad (\text{S61})$$

$$\Delta R_2(t) \sim \text{Binom}(R_2(t - \Delta t), 1 - \exp(-(\epsilon_{12}\text{FOI}_1(t) + \rho_2 + \mu)\Delta t)) \quad (\text{S62})$$

$$N_{R_2S}(t) \sim \text{Binom}\left(\Delta R_2(t), \frac{\rho_2}{\epsilon_{12}\text{FOI}_1(t) + \rho_2 + \mu}\right) \quad (\text{S63})$$

$$N_{R_2J_1}(t) \sim \text{Binom}\left(\Delta R_2(t), \frac{\epsilon_{12}\text{FOI}_1(t)}{\epsilon_{12}\text{FOI}_1(t) + \rho_2 + \mu}\right) \quad (\text{S64})$$

$$\Delta J_1(t) \sim \text{Binom}(J_1(t - \Delta t), 1 - \exp(-(\gamma_1 + \mu)\Delta t)) \quad (\text{S65})$$

$$N_{J_1R}(t) \sim \text{Binom}\left(\Delta J_1(t), \frac{\gamma_1}{\gamma_1 + \mu}\right) \quad (\text{S66})$$

$$\Delta J_2(t) \sim \text{Binom}(J_2(t - \Delta t), 1 - \exp(-(\gamma_2 + \mu)\Delta t)) \quad (\text{S67})$$

$$N_{J_2R}(t) \sim \text{Binom}\left(\Delta J_2(t), \frac{\gamma_2}{\gamma_2 + \mu}\right) \quad (\text{S68})$$

$$\Delta R(t) \sim \text{Binom}(R(t - \Delta t), 1 - \exp(-(\rho_1 + \rho_2 + \mu)\Delta t)) \quad (\text{S69})$$

$$N_{RR_1}(t) \sim \text{Binom}\left(\Delta R(t), \frac{\rho_1}{\rho_1 + \rho_2 + \mu}\right) \quad (\text{S70})$$

$$N_{RR_2}(t) \sim \text{Binom}\left(\Delta R(t), \frac{\rho_2}{\rho_1 + \rho_2 + \mu}\right) \quad (\text{S71})$$

$$S(t) = S(t - \Delta t) - \Delta S(t) + B(t) + N_{R_1S}(t) + N_{R_2S}(t) \quad (\text{S72})$$

$$I_1(t) = I_1(t - \Delta t) - \Delta I_1(t) + N_{SI_1}(t) \quad (\text{S73})$$

$$I_2(t) = I_2(t - \Delta t) - \Delta I_2(t) + N_{SI_2}(t) \quad (\text{S74})$$

$$R_1(t) = R_1(t - \Delta t) - \Delta R_1(t) + N_{I_1R_1}(t) + N_{RR_1}(t) \quad (\text{S75})$$

$$R_2(t) = R_2(t - \Delta t) - \Delta R_2(t) + N_{I_2R_2}(t) + N_{RR_2}(t) \quad (\text{S76})$$

$$J_1(t) = J_1(t - \Delta t) - \Delta J_1(t) + N_{R_2J_1}(t) \quad (\text{S77})$$

$$J_2(t) = J_2(t - \Delta t) - \Delta J_2(t) + N_{R_1J_2}(t) \quad (\text{S78})$$

$$R(t) = R(t - \Delta t) - \Delta R(t) + N_{J_1R}(t) + N_{J_2R}(t) \quad (\text{S79})$$

We simulated the model on a daily scale with previously estimated parameters for the RSV-HMPV interaction [34]:  $b_1 = 1.7/\text{weeks}$ ,  $b_2 = 1.95/\text{weeks}$ ,  $\theta_1 = 0.4$ ,  $\theta_2 = 0.3$ ,  $\phi_1 = 0.005 \times 7/364$ ,  $\phi_2 = 4.99 \times 7/364$ ,  $\epsilon_{12} = 0.92$ ,  $\epsilon_{21} = 0.45$ ,  $\gamma_1 = 1/10/\text{days}$ ,  $\gamma_2 = 1/10/\text{days}$ ,  $\rho_1 = 1/364/\text{days}$ ,  $\rho_2 = 1/364/\text{days}$ ,  $\mu = 1/(70 \times 364)/\text{days}$ , and  $N = 1 \times 10^8$ . The model was simulated from 1900 to 2030 assuming  $S(0) = N - 200$ ,  $I_1(0) = 100$ ,  $I_2(0) = 100$ ,  $R_1(0) = 0$ ,  $R_2(0) = 0$ ,  $J_1(0) = 0$ ,  $J_2(0) = 0$ , and  $R(0) = 0$ . The observed incidence for each strain is then simulated as follows:

$$C_1(t) = \text{Beta-Binom}(N_{SI_1}(t) + N_{R_2J_1}, \rho, k), \quad (\text{S80})$$

$$C_2(t) = \text{Beta-Binom}(N_{SI_2}(t) + N_{R_1J_2}, \rho, k), \quad (\text{S81})$$

where  $\rho$  represents the reporting probability and  $k$  represents the overdispersion parameter of beta-binomial distribution. We assumed  $\rho = 0.002$  (i.e., 0.2% probability) and  $k = 500$ . We also considered the total incidence:  $C_{\text{total}}(t) = C_1(t) + C_2(t)$ .

For both models, we considered a more realistically shaped pandemic perturbation  $\alpha(t)$  to challenge our ability to estimate the intervention effects. Thus, we

assumed a 40% transmission reduction for 3 months from March 2020, followed by a 10% transmission reduction for 6 months, 20% transmission reduction for 3 months, and a final return to normal levels:

$$\alpha(t) = \begin{cases} 1 & t < 2020.25 \\ 0.6 & 2020.25 \leq t < 2020.5 \\ 0.9 & 2020.5 \leq t < 2021 \\ 0.8 & 2021 \leq t < 2021.25 \\ 1 & 2021.25 \leq t \end{cases}. \quad (\text{S82})$$

For all simulations, we truncated the time series from the beginning of 2014 to the end of 2023 and aggregated them into weekly cases.

To infer intrinsic resilience from time series, we fitted a simple discrete time, deterministic SIRS model in a Bayesian framework [4]:

$$\Delta t = 1 \text{ week} \quad (\text{S83})$$

$$\text{FOI}(t) = \beta(t)(I(t - \Delta t) + \omega)/N \quad (\text{S84})$$

$$\Delta S(t) = [1 - \exp(-(\text{FOI}(t) + \mu)\Delta t)] S(t - \Delta t) \quad (\text{S85})$$

$$N_{SI}(t) = \frac{\text{FOI}(t)\Delta S(t)}{\text{FOI}(t) + \mu} \quad (\text{S86})$$

$$\Delta I(t) = [1 - \exp(-(\gamma + \mu)\Delta t)] I(t - \Delta t) \quad (\text{S87})$$

$$N_{IR}(t) = \frac{\gamma \Delta I(t)}{\gamma + \mu} \quad (\text{S88})$$

$$\Delta R(t) = [1 - \exp(-(\nu + \mu)\Delta t)] R(t - \Delta t) \quad (\text{S89})$$

$$N_{RS}(t) = \frac{\nu \Delta R(t)}{\nu + \mu} \quad (\text{S90})$$

$$S(t) = S(t - \Delta t) + \mu S - \Delta S(t) + N_{RS}(t) \quad (\text{S91})$$

$$I(t) = I(t - \Delta t) - \Delta I(t) + N_{SI}(t) \quad (\text{S92})$$

$$R(t) = R(t - \Delta t) - \Delta R(t) + N_{IR}(t) \quad (\text{S93})$$

where we include an extra term  $\omega$  to account for importation. Although actual simulations did not include any importation, we had found that including this term generally helped with model convergence in previous analyses [4]. The transmission rate was divided into a seasonal term  $\beta_{\text{seas}}(t)$  (repeated every year) and intervention term  $\alpha(t)$ , which were estimated jointly:

$$\beta(t) = \beta_{\text{seas}}(t)\alpha(t), \quad (\text{S94})$$

where  $\alpha < 1$  corresponds to reduction in transmission due to intervention effects. To constrain the smoothness of  $\beta_{\text{seas}}(t)$ , we imposed cyclic, random-walk priors:

$$\beta_{\text{seas}}(t) \sim \text{Normal}(\beta_{\text{seas}}(t - 1), \sigma) \quad t = 2 \dots 52 \quad (\text{S95})$$

$$\beta_{\text{seas}}(1) \sim \text{Normal}(\beta_{\text{seas}}(52), \sigma) \quad (\text{S96})$$

$$\sigma \sim \text{Half-Normal}(0, 1) \quad (\text{S97})$$

826 We fixed  $\alpha(t) = 1$  for all  $t < 2020$  and estimate  $\alpha$  assuming a normal prior:

$$\alpha \sim \text{Normal}(1, 0.25). \quad (\text{S98})$$

827 We assumed weakly informative priors on  $\omega$  and  $\nu$ :

$$\omega \sim \text{Half-Normal}(0, 200) \quad (\text{S99})$$

$$\nu \sim \text{Normal}(104, 26) \quad (\text{S100})$$

828 We assumed that the true birth/death rates, population sizes, and recovery rates  
829 are known. We note, however, that assuming  $\gamma = 1/\text{week}$  actually corresponds to  
830 a mean simulated infectious period of 1.6 weeks due to a time discretization, which  
831 is much longer than the true value; this approximation allows us to test whether we  
832 can still robustly estimate the intrinsic resilience given parameter mis-specification.  
833 Initial conditions were estimated with following priors:

$$S(0) = Ns(0) \quad (\text{S101})$$

$$I(0) = Ni(0) \quad (\text{S102})$$

$$s(0) \sim \text{Uniform}(0, 1) \quad (\text{S103})$$

$$i(0) \sim \text{Half-Normal}(0, 0.001) \quad (\text{S104})$$

834 Finally, the observation model was specified as follows:

$$\text{Cases}(t) \sim \text{Negative-Binomial}(\rho N_{SI}(t), \phi) \quad (\text{S105})$$

$$\rho \sim \text{Half-Normal}(0, 0.02) \quad (\text{S106})$$

$$\phi \sim \text{Half-Normal}(0, 10) \quad (\text{S107})$$

835 where  $\rho$  represents the reporting probability and  $\phi$  represents the negative binomial  
836 overdispersion parameter.

837 The model was fitted to four separate time series: (1) incidence time series from  
838 the SIRS model, (2) incidence time series for strain 1 from the two-strain model,  
839 (3) incidence time series for strain 2 from the two-strain model, and (4) combined  
840 incidence time series for strains 1 and 2 from the two-strain model. The model  
841 was fitted using rstan [49, 50] with 4 chains, each consisting of 2000 iterations.  
842 The resulting posterior distribution was used to calculate the intrinsic resilience of  
843 the seasonally unforced SIRS model with the same parameters; eigenvalues of the  
844 discrete-time SIR model were computed by numerically finding the equilibrium and  
845 calculating the Jacobian matrix.

846 **Validations for window-selection criteria**

847 We used stochastic SIRS simulations to identify optimal parameters for the window-  
 848 selection criteria that we used for the linear regression for estimating empirical re-  
 849 silience. For each simulation, we began by generating a random perturbation  $\alpha(t)$   
 850 from a random set of parameters. First, we drew the duration of perturbation  $\tau_{\text{npi}}$   
 851 from a uniform distribution between 1 and 2 years. Then, we drew independent  
 852 normal variables  $z_i$  of length  $[364\tau_{\text{npi}}]$  with a standard deviation of 0.02 and took a  
 853 reverse cumulative sum to obtain a realistic shape for the perturbation:

$$x_n = 1 + \sum_{i=n}^{[364\tau_{\text{npi}}]} z_i, \quad n = 1, \dots, [364\tau_{\text{npi}}]. \quad (\text{S108})$$

854 In contrast to simple perturbations that assume a constant reduction in transmis-  
 855 sion, this approach allows us to model transmission reduction that varies over time  
 856 smoothly. We repeated this random generation process until less than 10% of  $x_n$   
 857 exceeds 1—this was done to ensure the perturbation term  $\alpha(t)$  stays below 1 (and  
 858 therefore reduce transmission) for the most part. Then, we set any values that are  
 859 above 1 or below 0 to 1 and 0, respectively. Then, we randomly drew the minimum  
 860 transmission during perturbation  $\alpha_{\min}$  from a uniform distribution between 0.5 and  
 861 0.7 and scale  $x_n$  to have a minimum of  $\alpha_{\min}$ :

$$x_{\text{scale},n} = \alpha_{\min} + (1 - \alpha_{\min}) \times \frac{x_n - \min x_n}{1 - \min x_n}. \quad (\text{S109})$$

862 This allowed us to simulate a realistically shaped perturbation:

$$\alpha(t) = \begin{cases} 1 & t < 2020 \\ x_{\text{scale},364(t-2020)} & 2020 \leq t < 2020 + \tau_{\text{npi}} \\ 1 & \tau_{\text{npi}} \leq t \end{cases}. \quad (\text{S110})$$

863 Given this perturbation function, we draw  $\mathcal{R}_0$  from a uniform distribution between  
 864 1.5 and 4 and the mean duration of immunity  $1/\delta$  from a uniform distribution be-  
 865 tween 1 and 4. Then, we simulate the stochastic SIRS model from  $S(0) = 10^8/\mathcal{R}_0$   
 866 and  $I(0) = 100$  from 1990 to 2025 and truncate the time series to 2014–2025; if the  
 867 epidemic becomes extinct before the end of simulation, we discard that simulation  
 868 and start over from the perturbation generation step.

869 For each epidemic simulation, we computed the empirical resilience by varying  
 870 the threshold  $R$  for the nearest neighbor approach from 4 to 14 with increments of  
 871 2, the number of divisions  $K$  for the window selection between 8 and 25, and the  
 872 truncation threshold  $a$  for the window selection between 1 to 3; this was done for all  
 873 possible combinations of  $R$ ,  $K$ , and  $a$ . We also compared this with the naive approach  
 874 that uses the entire distance-from-attractor time series, starting from the maximum  
 875 distance to the end of the time series. We repeated this procedure 500 times and  
 876 quantified the correlation between empirical and intrinsic resilience estimates across  
 877 two approaches.

# Supplementary Figures

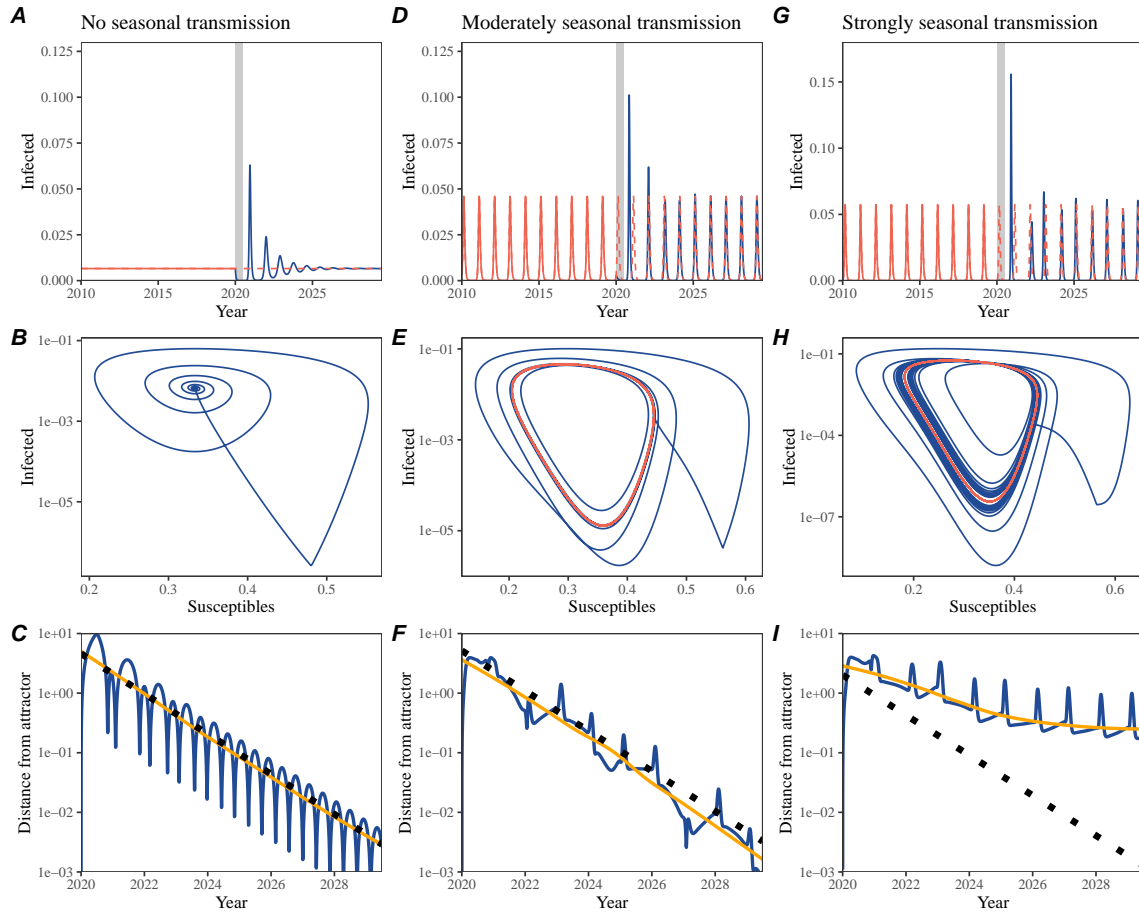


**Figure S1: Impact of seasonal transmission on pathogen resilience.** (A, D, G) Simulated epidemic trajectories using the SIRS model without seasonal forcing (A), with seasonal forcing of amplitude of 0.2 (D), and with seasonal forcing of amplitude of 0.4 (G). Red and blue solid lines represent epidemic dynamics before and after interventions are introduced, respectively. Red dashed lines represent counterfactual epidemic dynamics in the absence of interventions. Gray regions indicate the duration of interventions. (B, E, H) Phase plane representation of the time series in panels A, D, and G alongside the corresponding susceptible host dynamics. Red and blue solid lines represent epidemic trajectories on an SI phase plane before and after interventions are introduced, respectively. (C, F, I) Changes in logged distance from the attractor over time. Blue lines represent the logged distance from the attractor. Orange lines represent the locally estimated scatterplot smoothing (LOESS) fits to the logged distance from the attractor. Dotted lines show the intrinsic resilience of the seasonally unforced system.

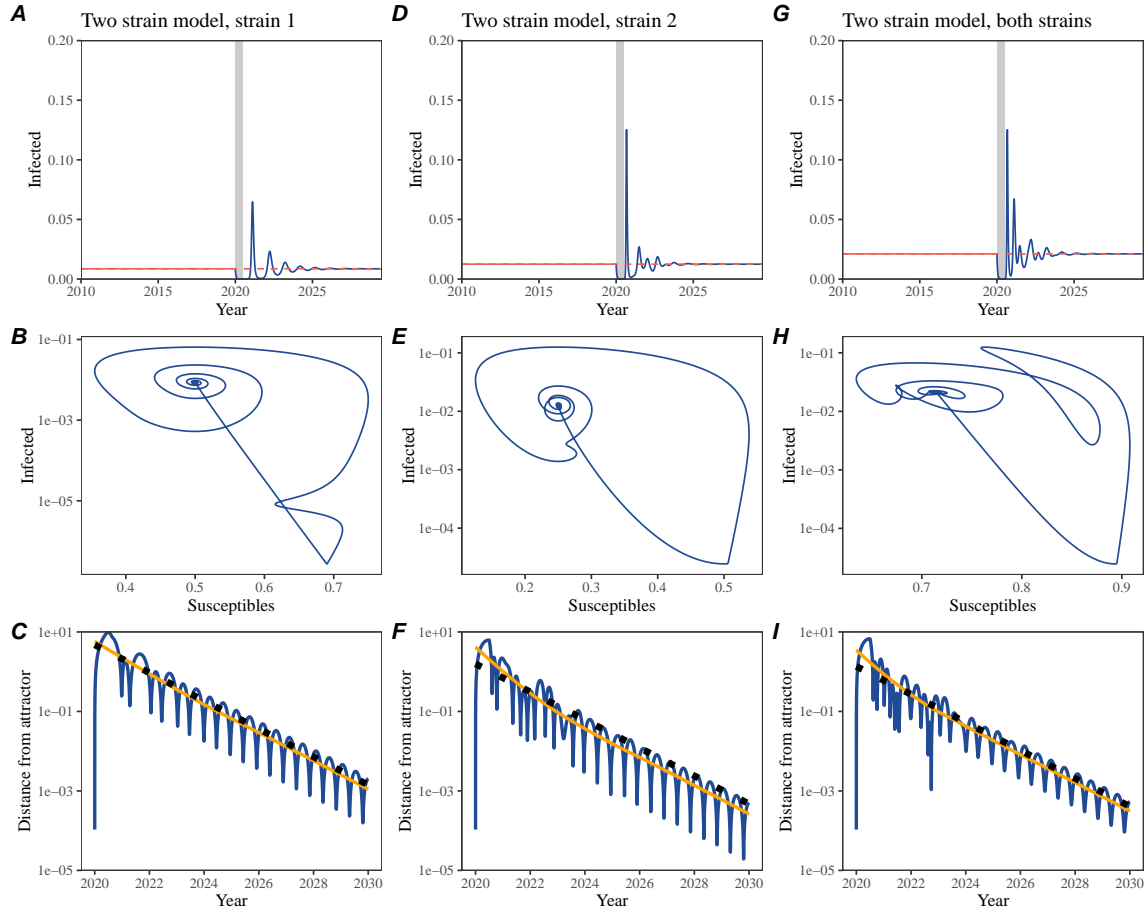


**Figure S2: A simple method to measure pathogen resilience following pandemic perturbations for a two-strain competition system without seasonal forcing.** (A, D, G) Simulated epidemic trajectories using a two-strain system without seasonal forcing. In this model, two strains compete through cross immunity. Red and blue solid lines represent epidemic dynamics before and after interventions are introduced, respectively. Red dashed lines represent counterfactual epidemic dynamics in the absence of interventions. Gray regions indicate the duration of interventions. (B, E, H) Phase plane representation of the time series in panels A, D, and G alongside the corresponding susceptible host dynamics. Blue solid lines represent epidemic trajectories on an SI phase plane before and after interventions are introduced, respectively. (C, F, I) Changes in logged distance from the attractor over time. Blue lines represent the logged distance from the attractor. Orange lines represent the locally estimated scatterplot smoothing (LOESS) fits to the logged distance from the attractor. Dotted lines show the intrinsic resilience of the seasonally unforced system.

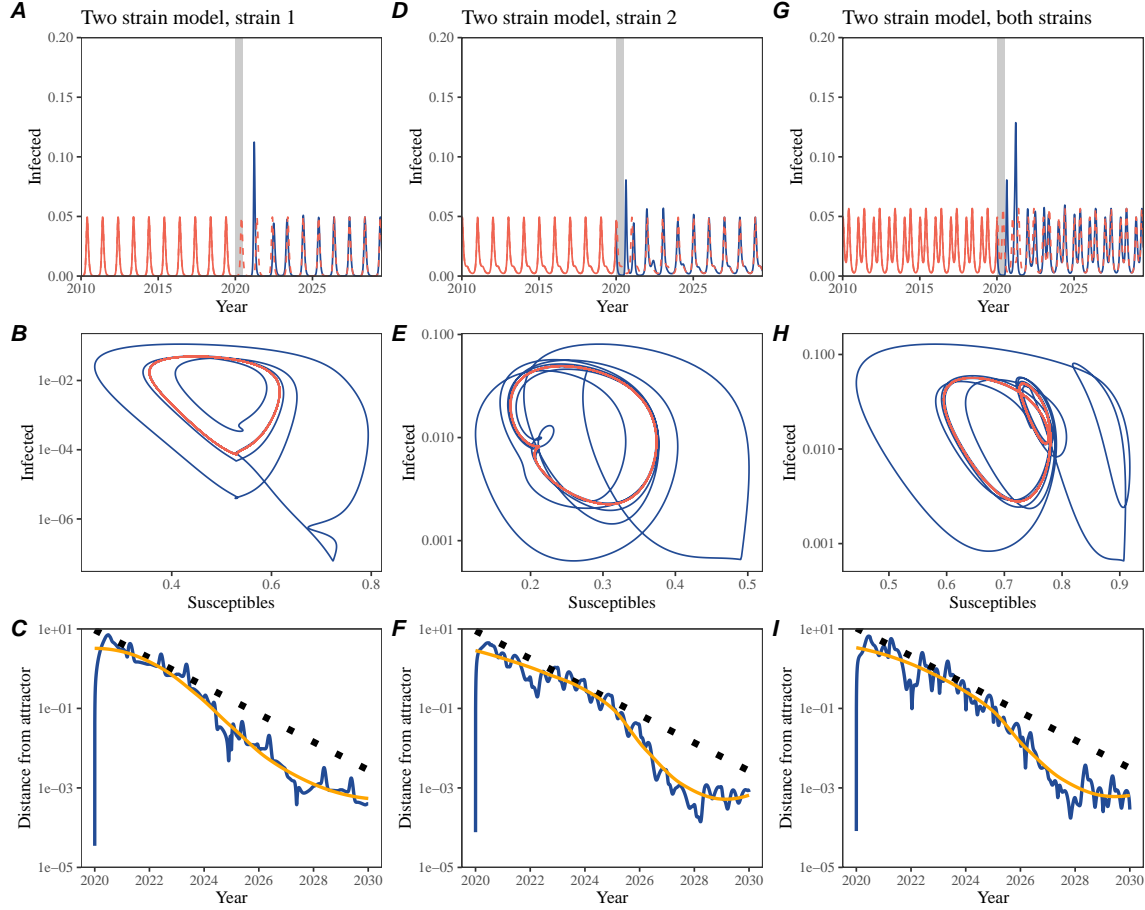


**Figure S3: A simple method to measure pathogen resilience following pandemic perturbations for a two-strain competition system with seasonal forcing.** (A, D, G) Simulated epidemic trajectories using a two-strain system with seasonal forcing (amplitude of 0.2). In this model, two strains compete through cross immunity. Red and blue solid lines represent epidemic dynamics before and after interventions are introduced, respectively. Red dashed lines represent counterfactual epidemic dynamics in the absence of interventions. Gray regions indicate the duration of interventions. (B, E, H) Phase plane representation of the time series in panels A, D, and G alongside the corresponding susceptible host dynamics. Red and blue solid lines represent epidemic trajectories on an SI phase plane before and after interventions are introduced, respectively. (C, F, I) Changes in logged distance from the attractor over time. Blue lines represent the logged distance from the attractor. Orange lines represent the locally estimated scatterplot smoothing (LOESS) fits to the logged distance from the attractor. Dotted lines show the intrinsic resilience of the seasonally unforced system.

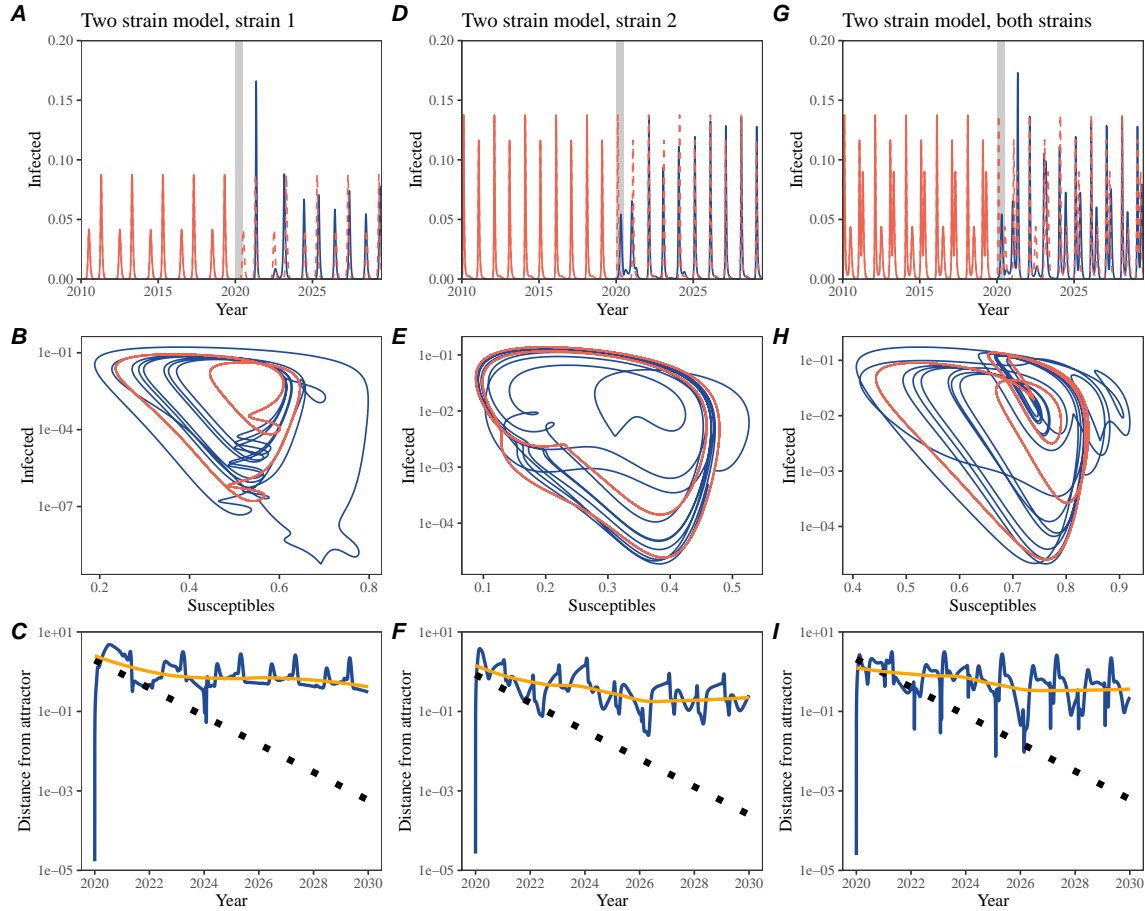


**Figure S4: A simple method to measure pathogen resilience following pandemic perturbations for a multi-strain competition system with strong seasonal forcing.** (A, D, G) Simulated epidemic trajectories using a two-strain system with seasonal forcing (amplitude of 0.2). In this model, two strains compete through cross immunity. Red and blue solid lines represent epidemic dynamics before and after interventions are introduced, respectively. Red dashed lines represent counterfactual epidemic dynamics in the absence of interventions. Gray regions indicate the duration of interventions. (B, E, H) Phase plane representation of the time series in panels A, D, and G alongside the corresponding susceptible host dynamics. Red and blue solid lines represent epidemic trajectories on an SI phase plane before and after interventions are introduced, respectively. (C, F, I) Changes in logged distance from the attractor over time. Blue lines represent the logged distance from the attractor. Orange lines represent the locally estimated scatterplot smoothing (LOESS) fits to the logged distance from the attractor. Dotted lines show the intrinsic resilience of the seasonally unforced system.

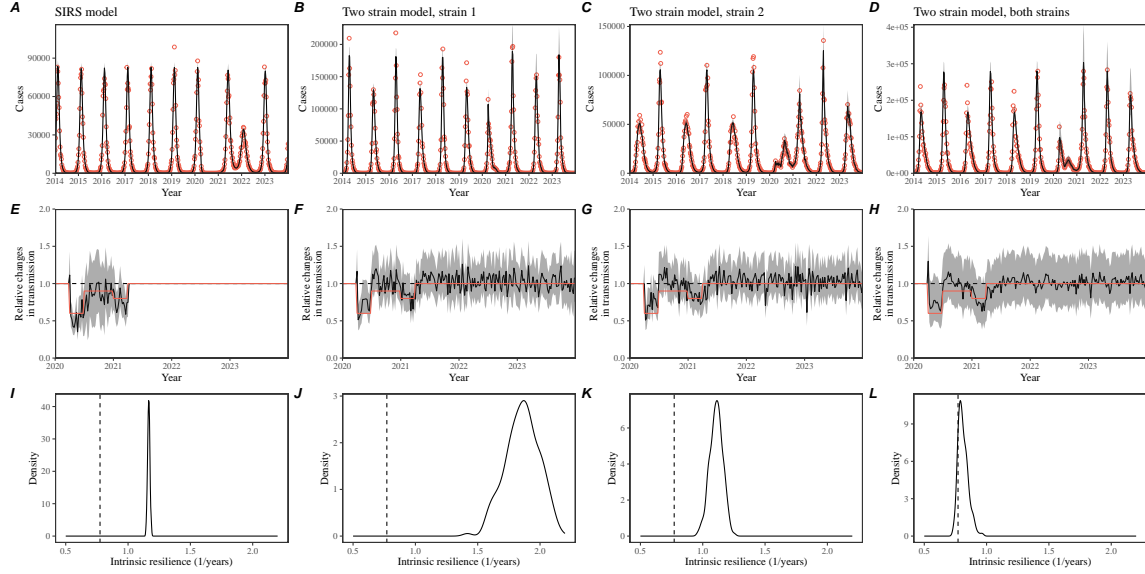


**Figure S5: Mechanistic model fits to simulated data and inferred intrinsic resilience.** We simulated discrete time, stochastic epidemic trajectories using a seasonally forced SIRS model (A,E,I) and a seasonally forced two-strain model (B–D, F–H, and J–L) and tested whether we can estimate the intrinsic resilience of the seasonally unforced versions of the model by fitting a mechanistic model (Supplementary Text). We fitted the same discrete time, one strain, deterministic SIRS model in each scenario. (A–D) Simulated case time series from corresponding models shown in the title (red) and SIRS model fits (black). (E–H) Assumed changes in transmission due to pandemic perturbations (red) and estimated time-varying relative transmission rates for the perturbation impact from the SIRS model fits (black). Solid lines and shaded regions represent fitted posterior median and 95% credible intervals. (I–L) Comparisons between the true and estimated intrinsic resilience of the seasonally unforced system. Vertical lines represent the true intrinsic resilience of the seasonally unforced system. Density plots represent the posterior distribution of the inferred intrinsic resilience of the seasonally unforced SIRS model using fitted parameters.

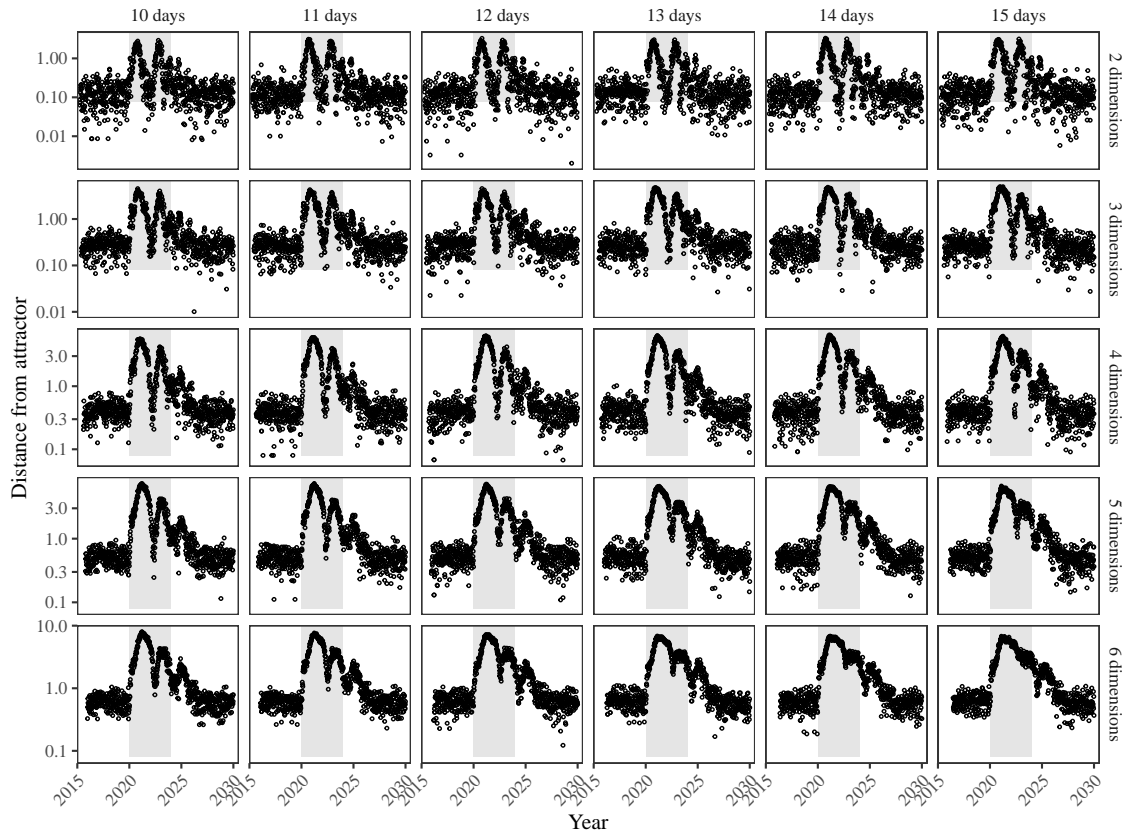


**Figure S6: Sensitivity of the distance from the attractor to choice of embedding lags and dimensions.** Sensitivity analysis for the distance-from-attractor time series shown in Figure 3E in the main text by varying the embedding lag between 10–15 days and embedding dimensions between 2–6 dimensions. The gray region represents the assumed period of pandemic perturbation.

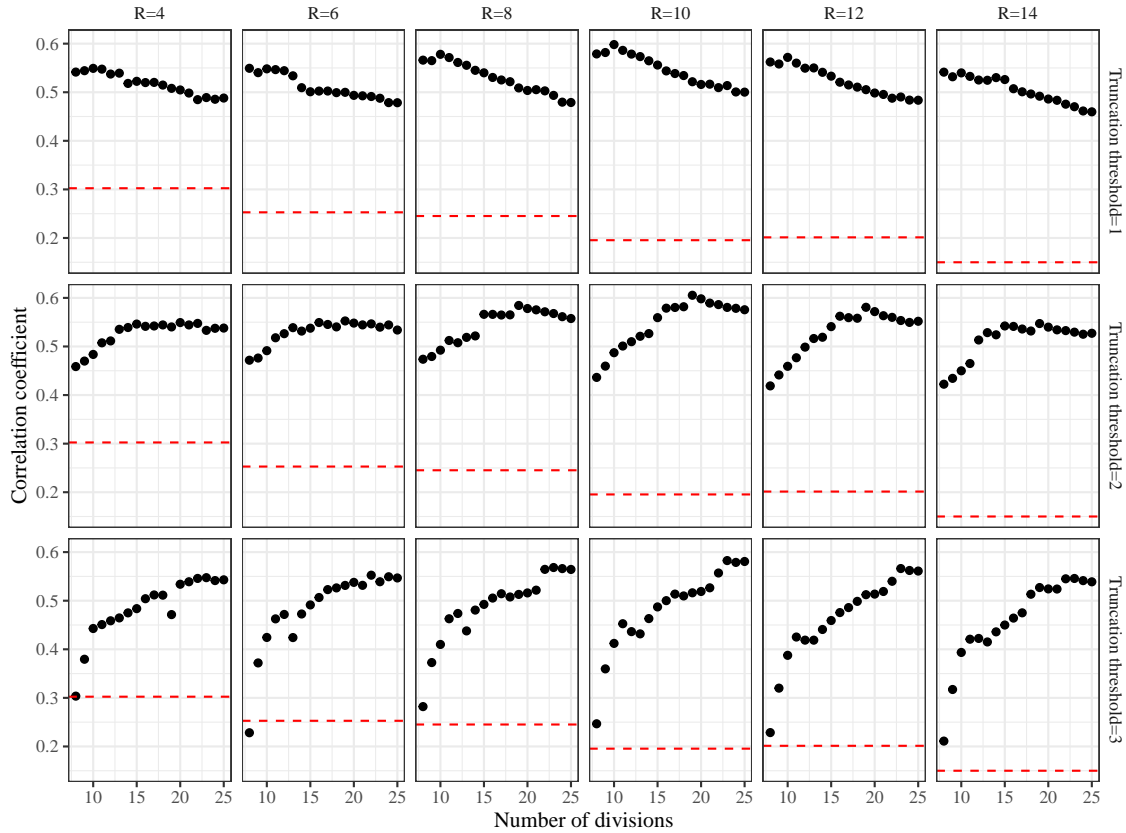


**Figure S7: Impact of fitting window selection on the estimation of empirical resilience.** We simulated 500 epidemics of a stochastic SIRS model with randomly drawn parameters and randomly generated pandemic perturbations (Supplementary Text). For each simulation, we varied the false nearest neighbor threshold  $R$  for reconstructing the empirical attractor as well as the parameters for regression window selection (i.e., the truncation threshold  $a$  and the number of divisions  $K$ ). Each point represents the resulting correlation coefficient between empirical and intrinsic resilience estimates for a given scenario. Dashed lines represent the correlation coefficient between empirical and intrinsic resilience estimates for the naive approach that fits a linear regression on a log scale, starting from the maximum distance until the end of the time series.

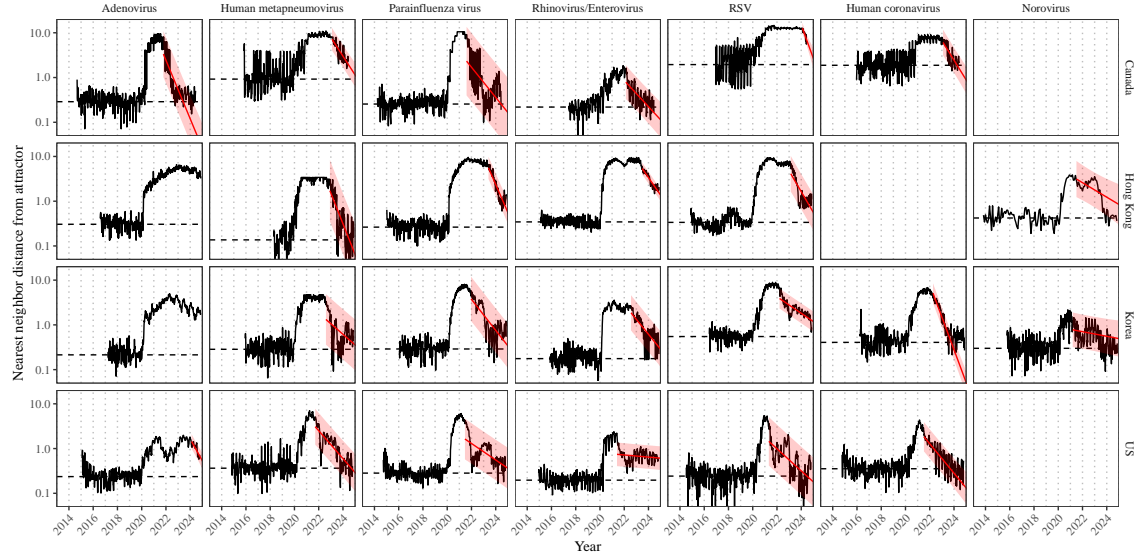


**Figure S8: Estimated time series of distance from the attractor for each pathogen and corresponding linear regression fits using automated window selection criteria across Canada, Hong Kong, Korea, and the US.** Black lines represent the estimated distance from the attractor. Red lines and shaded regions represent the linear regression fits and corresponding 95% confidence intervals. Dashed lines represent the average of the pre-pandemic nearest neighbor distances.

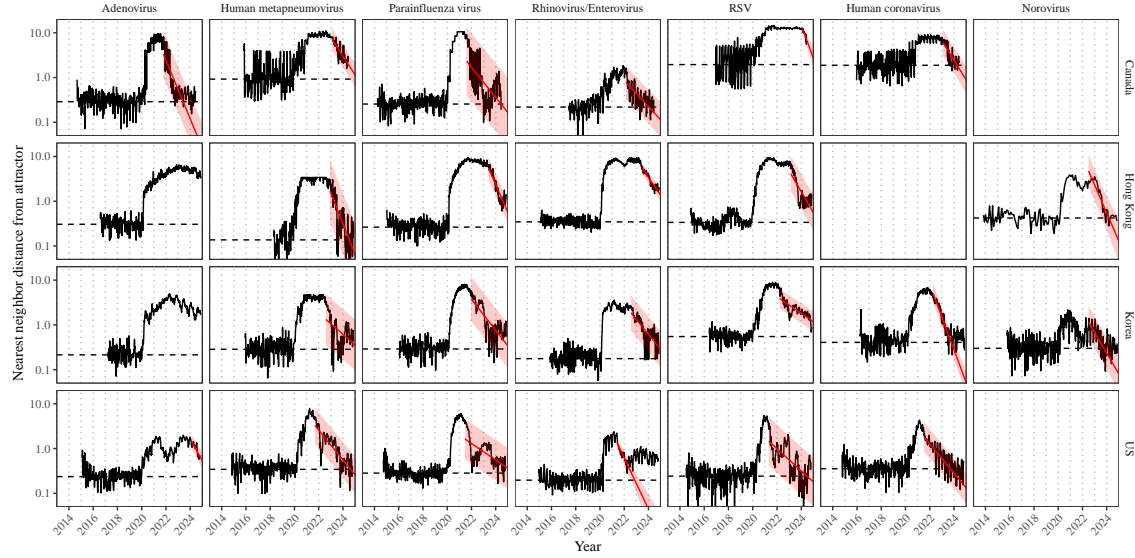


**Figure S9: Estimated time series of distance from the attractor for each pathogen and corresponding linear regression fits across Canada, Hong Kong, Korea, and the US, including ad-hoc regression window selection.** We used ad-hoc regression windows for norovirus in Hong Kong and Korea and rhinovirus/enterovirus in the US. Black lines represent the estimated distance from the attractor. Red lines and shaded regions represent the linear regression fits and corresponding 95% confidence intervals. Dashed lines represent the average of the pre-pandemic nearest neighbor distances.

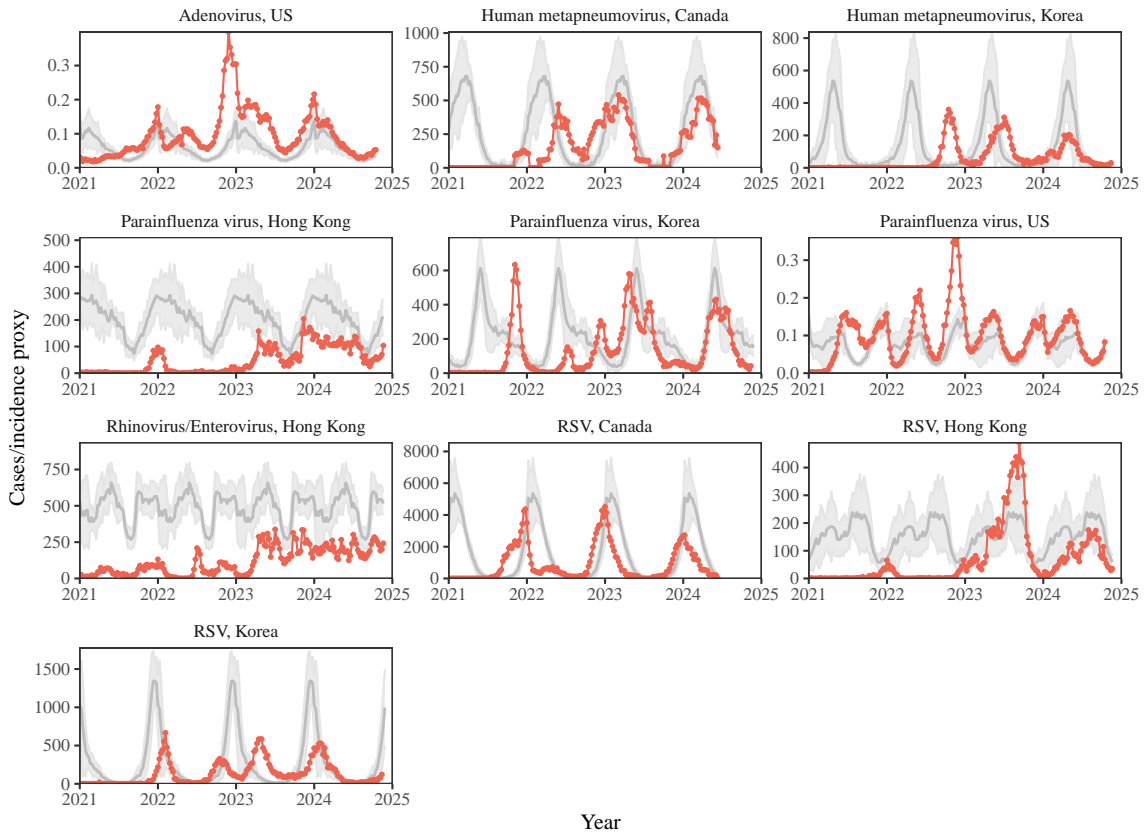


**Figure S10: Observed dynamics for pathogen that are predicted to return after the end of 2024.** Red points and lines represent data before 2020. Gray lines and shaded regions represent the mean seasonal patterns and corresponding 95% confidence intervals around the mean, previously shown in Figure 1.

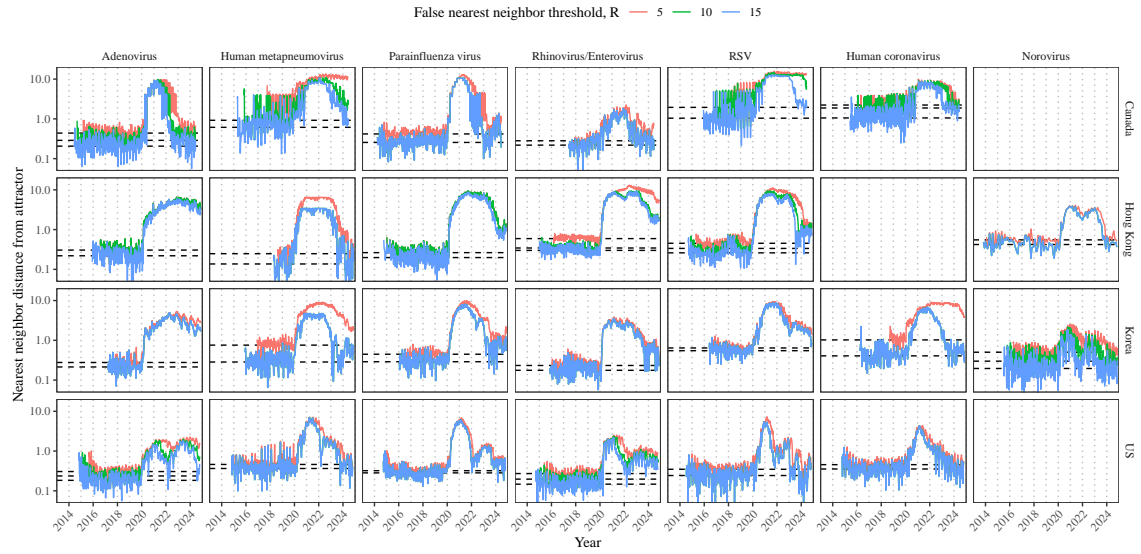


**Figure S11: Estimated time series of distance from the attractor for each pathogen across different choices about false nearest neighbor threshold values.** Using higher threshold values for the false nearest neighbor approach gives lower embedding dimensions. Colored lines represent the estimated distance from the attractor for different threshold values.

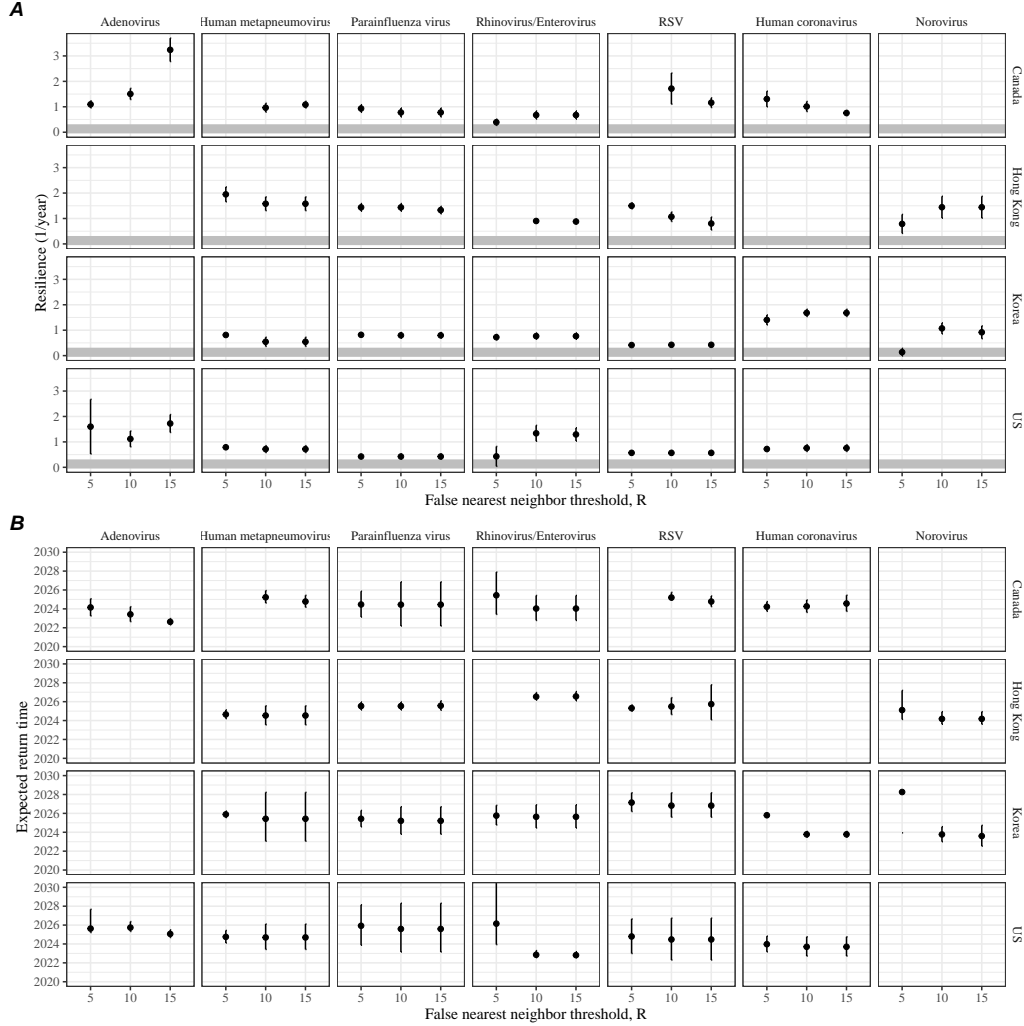


**Figure S12: Summary of resilience estimates and predictions for return time across different choices about false nearest neighbor threshold values.** The automated window selection method was used for all scenarios to estimate pathogen resilience, except for norovirus in Hong Kong and Korea and rhinovirus/enterovirus in the US. We used the same ad-hoc regression windows for norovirus in Hong Kong and Korea and rhinovirus/enterovirus in the US as we did in the main analysis. (A) Estimated pathogen resilience. The gray horizontal line represents the intrinsic resilience of pre-vaccination measles dynamics. (B) Predicted timing of when each pathogen will return to their pre-pandemic cycles. The dashed line in panel B indicates the end of 2024. Error bars represent 95% confidence intervals.

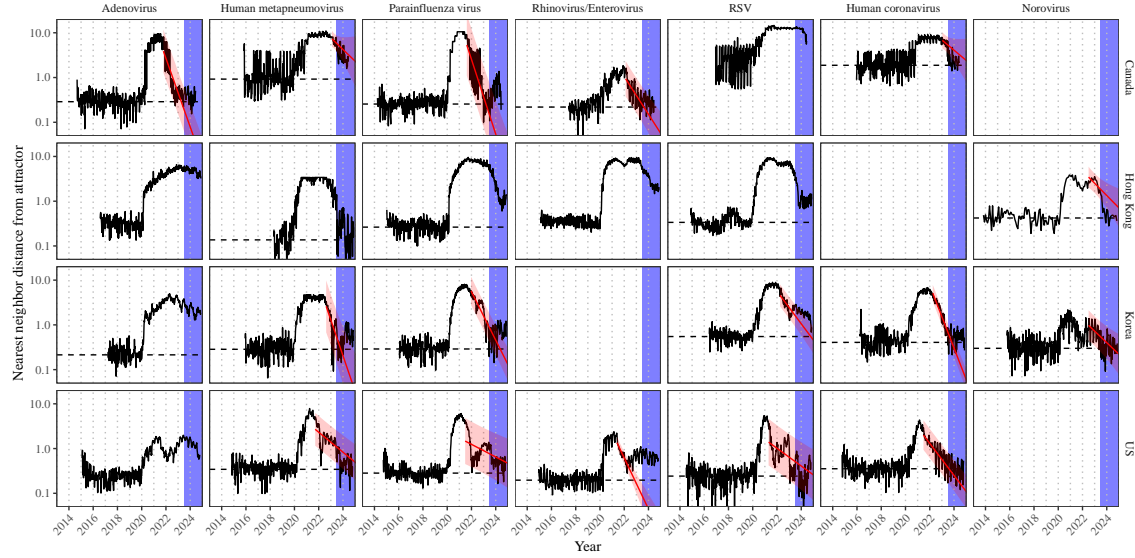


**Figure S13: Estimated time series of distance from the attractor for each pathogen and corresponding linear regression fits across Canada, Hong Kong, Korea, and the US based on data up to the 26th week of 2023.** We limited our data up to the 26th week of 2023 and applied the same regression approach as before. We used the same ad-hoc regression windows for norovirus in Hong Kong and Korea and rhinovirus/enterovirus in the US as the main analysis. Blue regions represent out of sample data. Black lines represent the estimated distance from the attractor. Red lines and shaded regions represent the linear regression fits and corresponding 95% confidence intervals. Dashed lines represent the average of the pre-pandemic nearest neighbor distances.

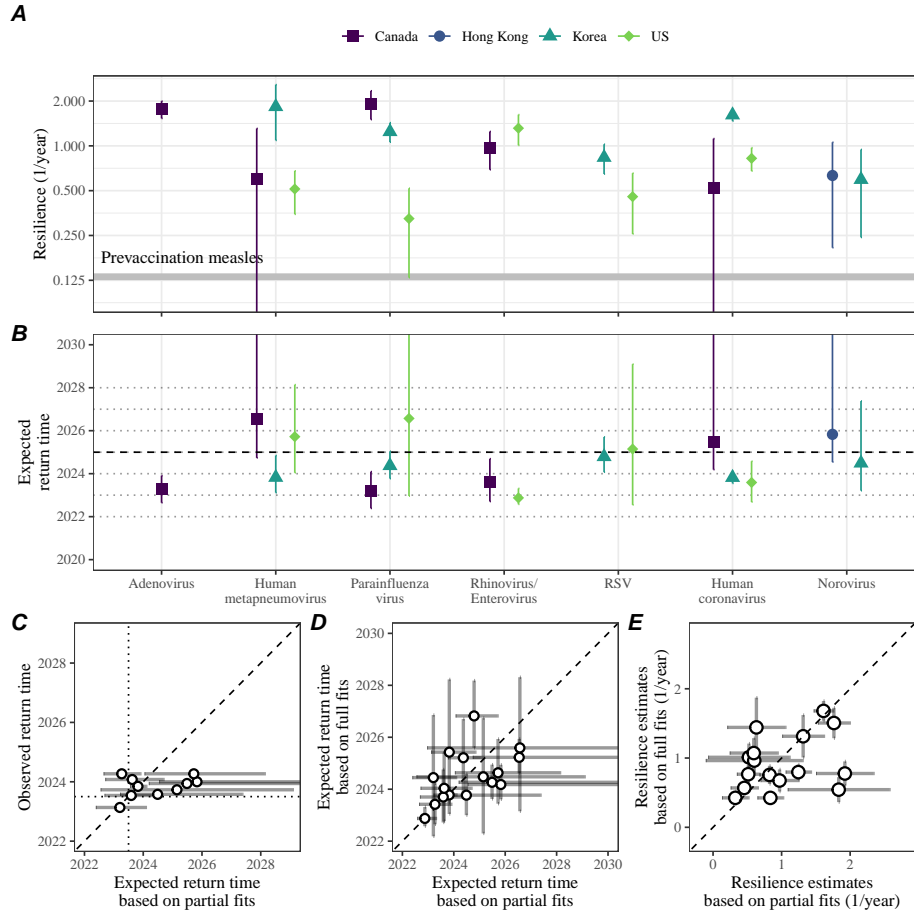


**Figure S14: Summary of resilience estimates and out-of-sample predictions for return time based on data up to the 26th week of 2023.** (A) Estimated pathogen resilience. The gray horizontal line represents the intrinsic resilience of pre-vaccination measles dynamics. (B) Predicted timing of when each pathogen will return to their pre-pandemic cycles. The dashed line in panel B indicates the end of 2024. Error bars represent 95% confidence intervals. (C) Comparisons between the predicted and observed return time. Vertical and horizontal dotted lines represent the 26th week of 2023; therefore, all predictions for points above this horizontal lines represent out-of-sample predictions. (D) Comparisons between predicted return times based on partial fits (based on data up to the 26th week of 2023) and full fits (based on all data). (E) Comparisons between resilience estimates based on partial fits (based on data up to the 26th week of 2023) and full fits (based on all data). Dashed lines represent the one-to-one line. Vertical and horizontal dotted lines

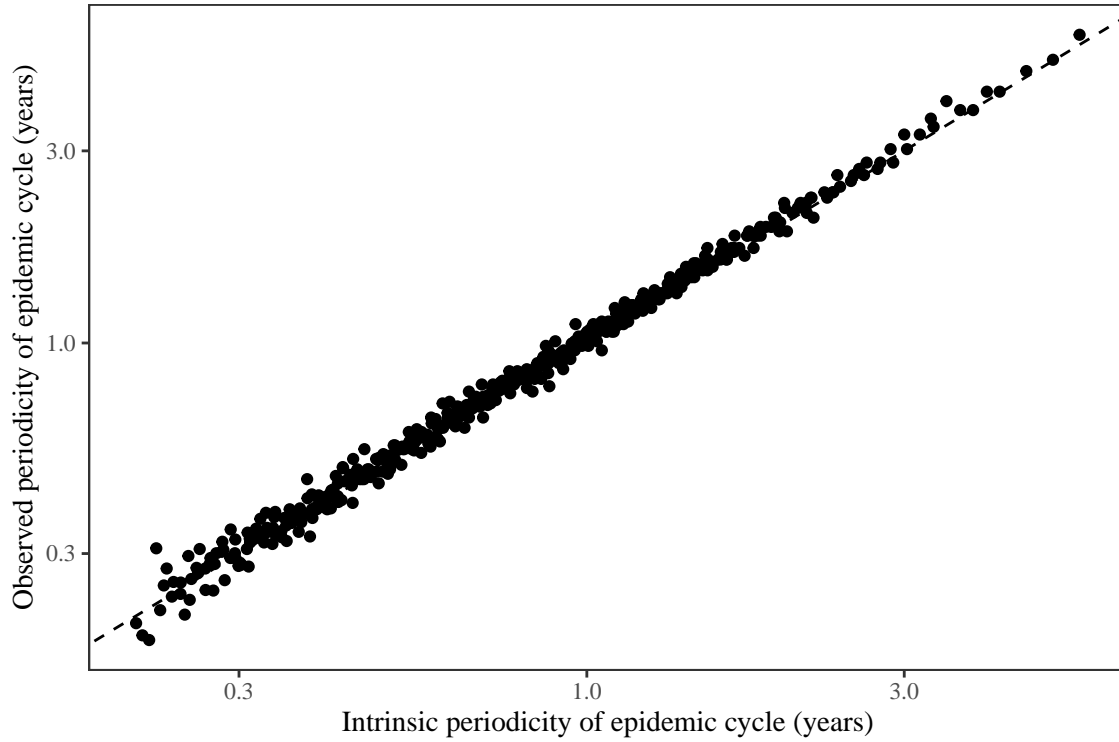


Figure S15: **Comparison between the observed and intrinsic periodicity of the epidemic cycle of the seasonally unforced SIRS model.** The observed periodicity of the epidemic corresponds to the periodicity at which maximum spectral density occurs. The intrinsic periodicity of the epidemic corresponds to  $2\pi/\text{Im}(\lambda)$ , where  $\text{Im}(\lambda)$  is the imaginary part of the eigenvalue.

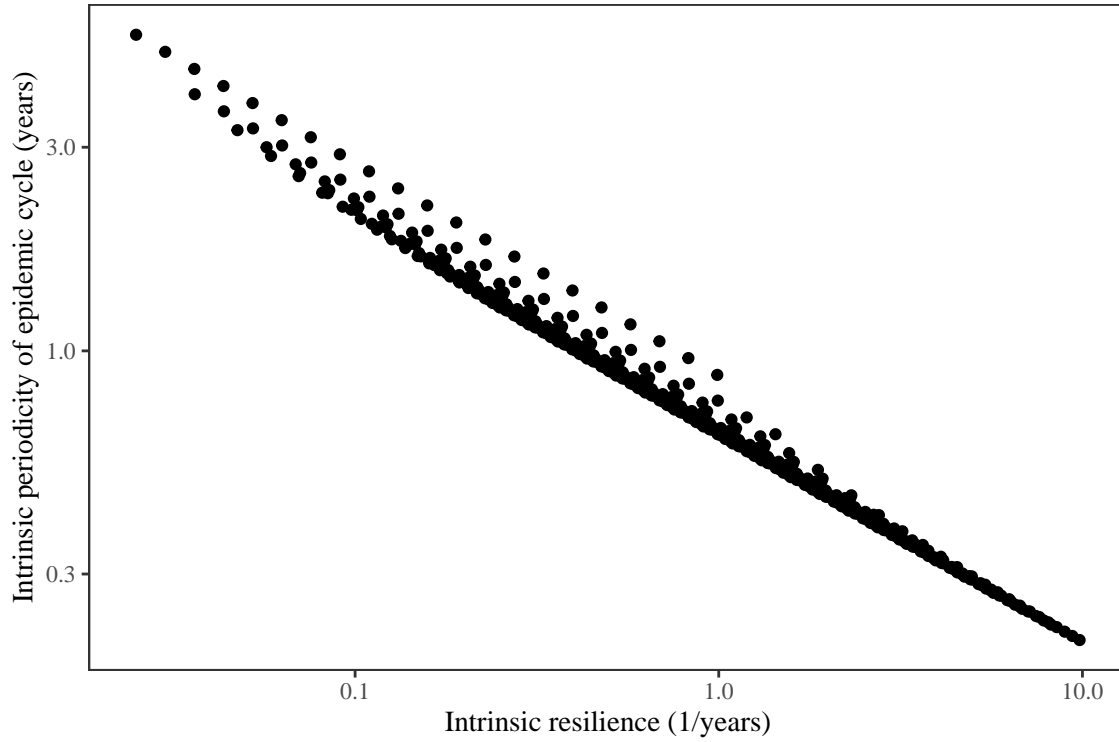
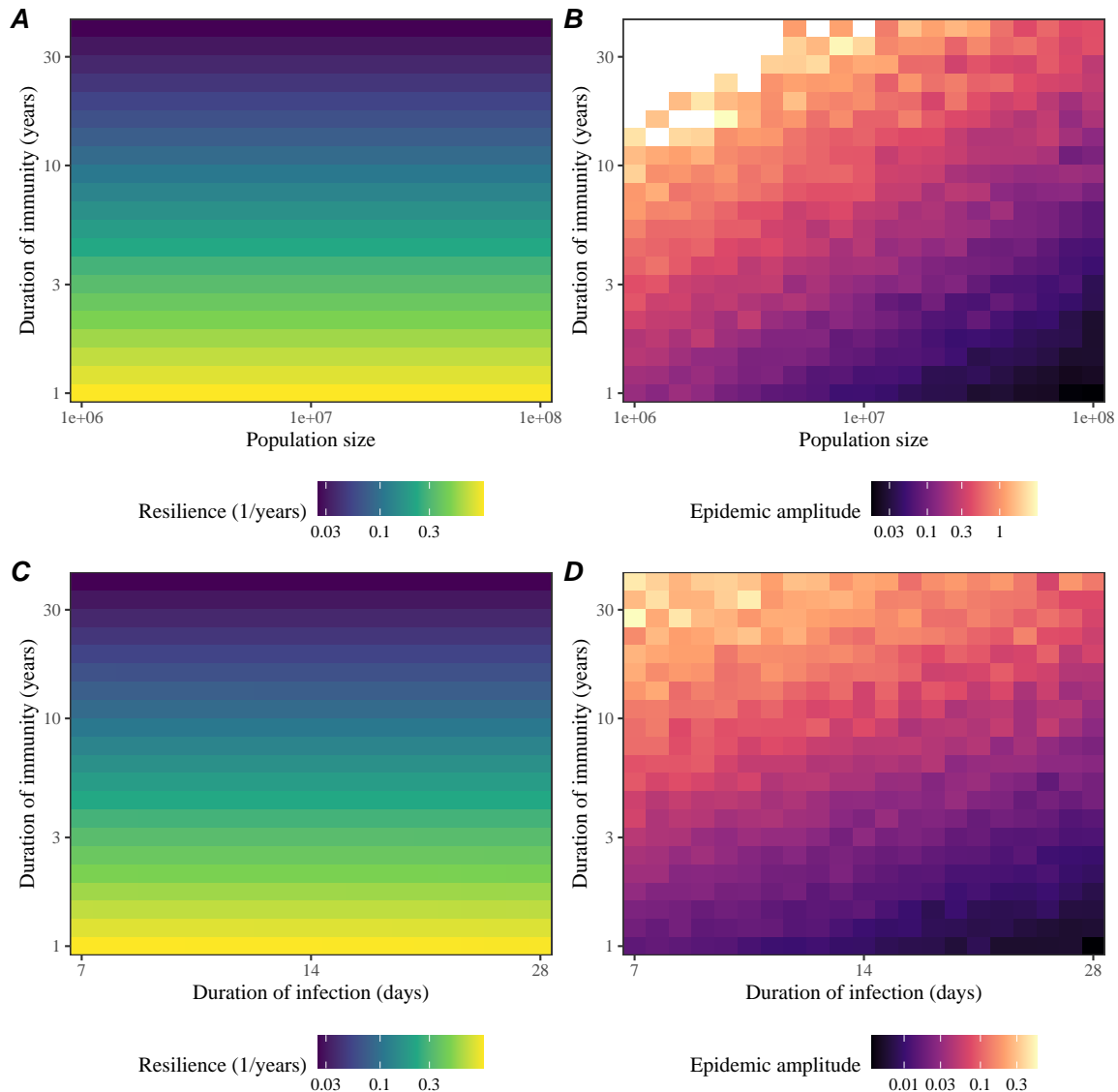
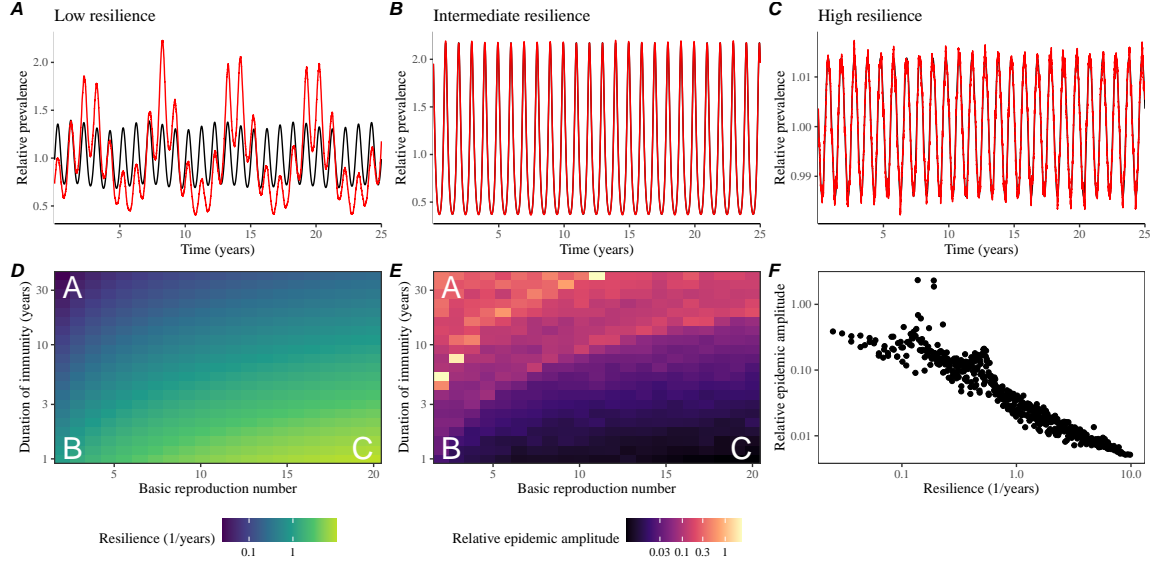


Figure S16: **Comparison between the intrinsic resilience and periodicity of the epidemic cycle of the seasonally unforced SIRS model.** The intrinsic resilience of the epidemic corresponds to the negative of the real value of the eigenvalue  $-\text{Re}(\lambda)$ . The intrinsic periodicity of the epidemic corresponds to  $2\pi/\text{Im}(\lambda)$ , where  $\text{Im}(\lambda)$  is the imaginary part of the eigenvalue.



**Figure S17: Impact of population size and the average duration of infection of a host-pathogen system on its sensitivity to stochastic perturbations.** (A) Intrinsic resilience of a system as a function of population size and the average duration of immunity. (B) Epidemic amplitude as a function of population size and the average duration of immunity. (C) Intrinsic resilience of a system as a function of the average duration of infection and immunity. (D) Epidemic amplitude as a function of the average duration of infection and immunity. The epidemic amplitude corresponds to  $(\max I - \min I)/(2\bar{I})$ , where  $\bar{I}$  represents the mean prevalence.



**Figure S18: Linking resilience of a host-pathogen system to its sensitivity to stochastic perturbations for the seasonally forced SIRS model.** (A–C) Epidemic trajectories of a stochastic SIRS model with demographic stochasticity across three different resilience values: low, intermediate, and high. The relative prevalence was calculated by dividing infection prevalence by its mean value. Black lines represent deterministic epidemic trajectories. Red lines represent stochastic epidemic trajectories. (D) The intrinsic resilience of the seasonally unforced system as a function of the basic reproduction number  $\mathcal{R}_0$  and the duration of immunity. (E) The relative epidemic amplitude, a measure of sensitivity to stochastic perturbations, as a function of the basic reproduction number  $\mathcal{R}_0$  and the duration of immunity. To calculate the relative epidemic amplitude, we first take the relative difference in infection prevalence between stochastic and deterministic trajectories:  $\epsilon = (I_{\text{stoch}} - I_{\text{det}})/I_{\text{det}}$ . Then, we calculate the difference between maximum and minimum of the relative difference and divide by half:  $(\max \epsilon - \min \epsilon)/2$ . Labels A–C in panels D and E correspond to scenarios shown in panels A–C. (F) The relationship between pathogen resilience and relative epidemic amplitude.

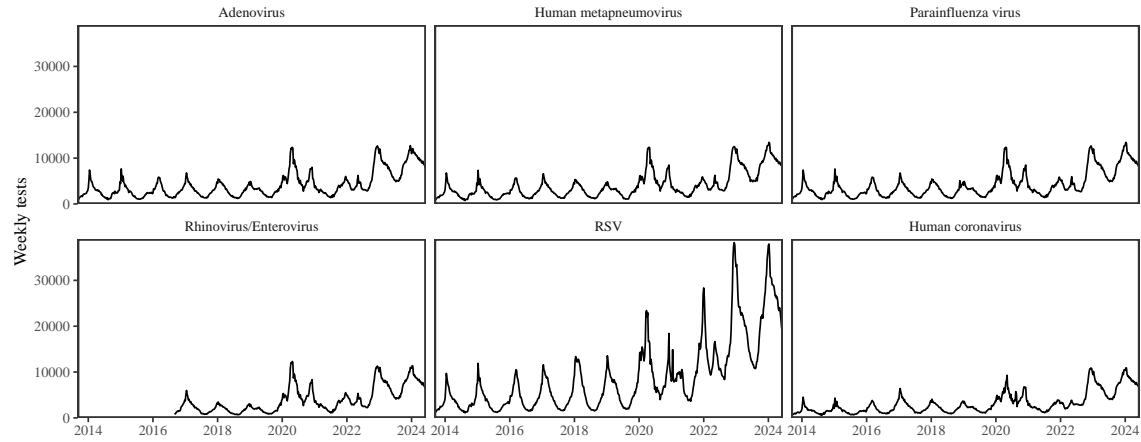


Figure S19: Testing patterns for respiratory pathogens in Canada.

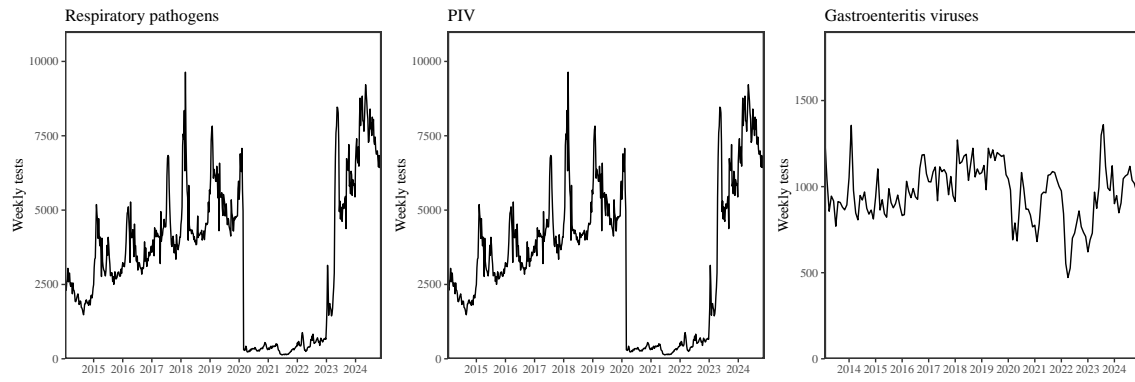


Figure S20: Testing patterns for respiratory pathogens, PIV, and gastroenteritis viruses in Hong Kong.

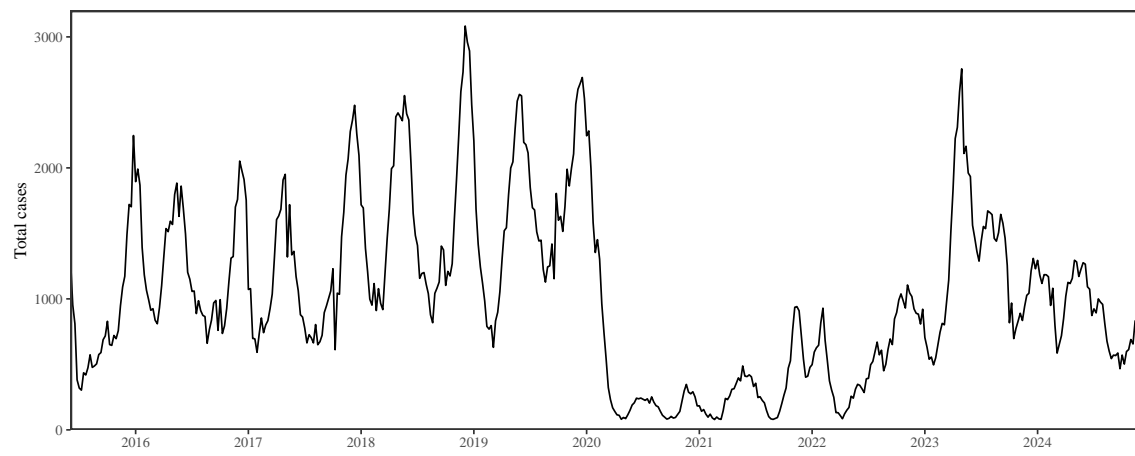


Figure S21: Total number of reported respiratory infection cases in Korea.

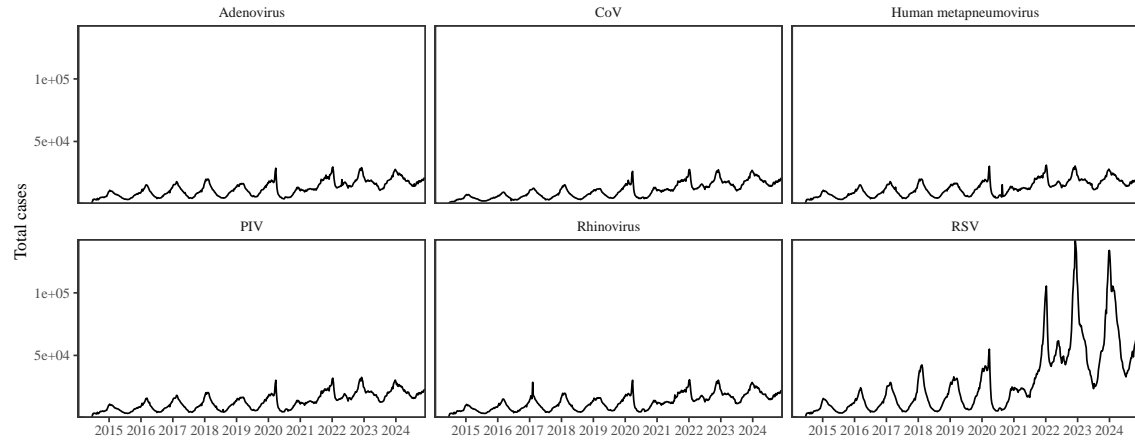


Figure S22: Testing patterns for respiratory pathogens in the US reported through the NREVSS.

## 879 References

- 880 [1] Rachel E Baker, Sang Woo Park, Wenchang Yang, Gabriel A Vecchi, C Jessica E  
881 Metcalf, and Bryan T Grenfell. The impact of COVID-19 nonpharmaceutical  
882 interventions on the future dynamics of endemic infections. *Proceedings of the*  
883 *National Academy of Sciences*, 117(48):30547–30553, 2020.
- 884 [2] Gabriela B Gomez, Cedric Mahé, and Sandra S Chaves. Uncertain effects of the  
885 pandemic on respiratory viruses. *Science*, 372(6546):1043–1044, 2021.
- 886 [3] Mihaly Koltai, Fabienne Krauer, David Hodgson, Edwin van Leeuwen, Marina  
887 Treskova-Schwarzbach, Mark Jit, and Stefan Flasche. Determinants of RSV  
888 epidemiology following suppression through pandemic contact restrictions. *Epi-*  
889 *demics*, 40:100614, 2022.
- 890 [4] Sang Woo Park, Brooklyn Noble, Emily Howerton, Bjarke F Nielsen, Sarah  
891 Lentz, Lilliam Ambroggio, Samuel Dominguez, Kevin Messacar, and Bryan T  
892 Grenfell. Predicting the impact of non-pharmaceutical interventions against  
893 COVID-19 on *Mycoplasma pneumoniae* in the United States. *Epidemics*,  
894 49:100808, 2024.
- 895 [5] Amanda C Perofsky, Chelsea L Hansen, Roy Burstein, Shanda Boyle, Robin  
896 Prentice, Cooper Marshall, David Reinhart, Ben Capodanno, Melissa Truong,  
897 Kristen Schwabe-Fry, et al. Impacts of human mobility on the citywide trans-  
898 mission dynamics of 18 respiratory viruses in pre-and post-COVID-19 pandemic  
899 years. *Nature communications*, 15(1):4164, 2024.
- 900 [6] Eric J Chow, Timothy M Uyeki, and Helen Y Chu. The effects of the COVID-19  
901 pandemic on community respiratory virus activity. *Nature Reviews Microbiol-*  
902 *ogy*, 21(3):195–210, 2023.
- 903 [7] Stephen M Kissler, Christine Tedijanto, Edward Goldstein, Yonatan H Grad,  
904 and Marc Lipsitch. Projecting the transmission dynamics of SARS-CoV-2  
905 through the postpandemic period. *Science*, 368(6493):860–868, 2020.
- 906 [8] Rachel E Baker, Chadi M Saad-Roy, Sang Woo Park, Jeremy Farrar, C Jessica E  
907 Metcalf, and Bryan T Grenfell. Long-term benefits of nonpharmaceutical inter-  
908 ventions for endemic infections are shaped by respiratory pathogen dynamics.  
909 *Proceedings of the National Academy of Sciences*, 119(49):e2208895119, 2022.
- 910 [9] Maaike C Swets, Clark D Russell, Ewen M Harrison, Annemarie B Docherty,  
911 Nazir Lone, Michelle Girvan, Hayley E Hardwick, Leonardus G Visser, Pe-  
912 ter JM Openshaw, Geert H Groeneveld, et al. SARS-CoV-2 co-infection with  
913 influenza viruses, respiratory syncytial virus, or adenoviruses. *The Lancet*,  
914 399(10334):1463–1464, 2022.

- 915 [10] Chun-Yang Lin, Joshua Wolf, David C Brice, Yilun Sun, Macauley Locke,  
916 Sean Cherry, Ashley H Castellaw, Marie Wehenkel, Jeremy Chase Crawford,  
917 Veronika I Zarnitsyna, et al. Pre-existing humoral immunity to human common  
918 cold coronaviruses negatively impacts the protective SARS-CoV-2 antibody re-  
919 sponse. *Cell host & microbe*, 30(1):83–96, 2022.
- 920 [11] Sam M Murray, Azim M Ansari, John Frater, Paul Klenerman, Susanna  
921 Dunachie, Eleanor Barnes, and Ane Ogbe. The impact of pre-existing cross-  
922 reactive immunity on SARS-CoV-2 infection and vaccine responses. *Nature*  
923 *Reviews Immunology*, 23(5):304–316, 2023.
- 924 [12] John-Sebastian Eden, Chisha Sikazwe, Ruopeng Xie, Yi-Mo Deng, Sheena G  
925 Sullivan, Alice Michie, Avram Levy, Elena Cutmore, Christopher C Blyth,  
926 Philip N Britton, et al. Off-season RSV epidemics in Australia after easing  
927 of COVID-19 restrictions. *Nature communications*, 13(1):2884, 2022.
- 928 [13] Stuart L Pimm. The structure of food webs. *Theoretical population biology*,  
929 16(2):144–158, 1979.
- 930 [14] Michael G Neubert and Hal Caswell. Alternatives to resilience for measuring  
931 the responses of ecological systems to perturbations. *Ecology*, 78(3):653–665,  
932 1997.
- 933 [15] Lance H Gunderson. Ecological resilience—in theory and application. *Annual*  
934 *review of ecology and systematics*, 31(1):425–439, 2000.
- 935 [16] Vasilis Dakos and Sonia Kéfi. Ecological resilience: what to measure and how.  
936 *Environmental Research Letters*, 17(4):043003, 2022.
- 937 [17] Floris Takens. Detecting strange attractors in turbulence. In *Dynamical Sys-*  
938 *tems and Turbulence, Warwick 1980: proceedings of a symposium held at the*  
939 *University of Warwick 1979/80*, pages 366–381. Springer, 2006.
- 940 [18] Jonathan Dushoff, Joshua B Plotkin, Simon A Levin, and David JD Earn.  
941 Dynamical resonance can account for seasonality of influenza epidemics. *Pro-*  
942 , 101(48):16915–16916, 2004.
- 943 [19] Alan Hastings, Carole L Hom, Stephen Ellner, Peter Turchin, and H Charles J  
944 Godfray. Chaos in ecology: is mother nature a strange attractor? *Annual review*  
945 *of ecology and systematics*, pages 1–33, 1993.
- 946 [20] Alan Hastings, Karen C Abbott, Kim Cuddington, Tessa Francis, Gabriel Gell-  
947 ner, Ying-Cheng Lai, Andrew Morozov, Sergei Petrovskii, Katherine Scran-  
948 ton, and Mary Lou Zeeman. Transient phenomena in ecology. *Science*,  
949 361(6406):eaat6412, 2018.

- 950 [21] Matthew B Kennel, Reggie Brown, and Henry DI Abarbanel. Determining  
951 embedding dimension for phase-space reconstruction using a geometrical con-  
952 struction. *Physical review A*, 45(6):3403, 1992.
- 953 [22] Eugene Tan, Shannon Algar, Débora Corrêa, Michael Small, Thomas Stemler,  
954 and David Walker. Selecting embedding delays: An overview of embedding  
955 techniques and a new method using persistent homology. *Chaos: An Interdis-*  
956 *ciplinary Journal of Nonlinear Science*, 33(3), 2023.
- 957 [23] Bjarke Frost Nielsen, Sang Woo Park, Emily Howerton, Olivia Frost Lorentzen,  
958 Mogens H Jensen, and Bryan T Grenfell. Complex multiannual cycles of My-  
959 coplasma pneumoniae: persistence and the role of stochasticity. *arXiv*, 2025.
- 960 [24] Samantha Bosis, Susanna Esposito, HGM Niesters, GV Zuccotti, G Marseglia,  
961 Marcello Lanari, Giovanna Zuin, C Pelucchi, ADME Osterhaus, and Nicola  
962 Principi. Role of respiratory pathogens in infants hospitalized for a first episode  
963 of wheezing and their impact on recurrences. *Clinical microbiology and infection*,  
964 14(7):677–684, 2008.
- 965 [25] Miguel L O’Ryan, Yalda Lucero, Valeria Prado, María Elena Santolaya, Marcela  
966 Rabello, Yanahara Solis, Daniela Berriós, Miguel A O’Ryan-Soriano, Hector  
967 Cortés, and Nora Mamani. Symptomatic and asymptomatic rotavirus and  
968 norovirus infections during infancy in a Chilean birth cohort. *The Pediatric  
969 infectious disease journal*, 28(10):879–884, 2009.
- 970 [26] Virginia E Pitzer, Cécile Viboud, Vladimir J Alonso, Tanya Wilcox, C Jessica  
971 Metcalf, Claudia A Steiner, Amber K Haynes, and Bryan T Grenfell. Environmental  
972 drivers of the spatiotemporal dynamics of respiratory syncytial virus in  
973 the United States. *PLoS pathogens*, 11(1):e1004591, 2015.
- 974 [27] Arthur WD Edridge, Joanna Kaczorowska, Alexis CR Hoste, Margreet Bakker,  
975 Michelle Klein, Katherine Loens, Maarten F Jebbink, Amy Matser, Cormac M  
976 Kinsella, Paloma Rueda, et al. Seasonal coronavirus protective immunity is  
977 short-lasting. *Nature medicine*, 26(11):1691–1693, 2020.
- 978 [28] Jennifer M Radin, Anthony W Hawksworth, Peter E Kammerer, Melinda Bal-  
979 ansay, Rema Raman, Suzanne P Lindsay, and Gary T Brice. Epidemiology  
980 of pathogen-specific respiratory infections among three US populations. *PLoS  
981 One*, 9(12):e114871, 2014.
- 982 [29] Guojian Lv, Limei Shi, Yi Liu, Xuecheng Sun, and Kai Mu. Epidemiological  
983 characteristics of common respiratory pathogens in children. *Scientific Reports*,  
984 14(1):16299, 2024.
- 985 [30] Saverio Caini, Adam Meijer, Marta C Nunes, Laetitia Henaff, Malaika Zounon,  
986 Bronke Boudewijns, Marco Del Riccio, and John Paget. Probable extinction of

987 influenza b/yamagata and its public health implications: a systematic literature  
988 review and assessment of global surveillance databases. *The Lancet Microbe*,  
989 2024.

990 [31] Zhiyuan Chen, Joseph L-H Tsui, Bernardo Gutierrez, Simon Busch Moreno,  
991 Louis du Plessis, Xiaowei Deng, Jun Cai, Sumali Bajaj, Marc A Suchard,  
992 Oliver G Pybus, et al. COVID-19 pandemic interventions reshaped the global  
993 dispersal of seasonal influenza viruses. *Science*, 386(6722):eadq3003, 2024.

994 [32] Hai Nguyen-Tran, Sang Woo Park, Kevin Messacar, Samuel R Dominguez,  
995 Matthew R Vogt, Sallie Permar, Perdita Permaul, Michelle Hernandez, Daniel C  
996 Douek, Adrian B McDermott, et al. Enterovirus D68: a test case for the use of  
997 immunological surveillance to develop tools to mitigate the pandemic potential  
998 of emerging pathogens. *The Lancet Microbe*, 3(2):e83–e85, 2022.

999 [33] Bryan T Grenfell, Ottar N Bjørnstad, and Bärbel F Finkenstädt. Dynamics of  
1000 measles epidemics: scaling noise, determinism, and predictability with the TSIR  
1001 model. *Ecological monographs*, 72(2):185–202, 2002.

1002 [34] Samit Bhattacharyya, Per H Gesteland, Kent Korgenski, Ottar N Bjørnstad,  
1003 and Frederick R Adler. Cross-immunity between strains explains the dynamical  
1004 pattern of paramyxoviruses. *Proceedings of the National Academy of Sciences*,  
1005 112(43):13396–13400, 2015.

1006 [35] Katharine R Dean, Fabienne Krauer, Lars Walløe, Ole Christian Lingjærde, Bar-  
1007 Barbara Bramanti, Nils Chr Stenseth, and Boris V Schmid. Human ectoparasites  
1008 and the spread of plague in Europe during the Second Pandemic. *Proceedings  
1009 of the National Academy of Sciences*, 115(6):1304–1309, 2018.

1010 [36] Margarita Pons-Salort and Nicholas C Grassly. Serotype-specific immunity  
1011 explains the incidence of diseases caused by human enteroviruses. *Science*,  
1012 361(6404):800–803, 2018.

1013 [37] Sarah Cobey and Edward B Baskerville. Limits to causal inference with state-  
1014 space reconstruction for infectious disease. *PloS one*, 11(12):e0169050, 2016.

1015 [38] P Rohani, CJ Green, NB Mantilla-Beniers, and Bryan T Grenfell. Ecological  
1016 interference between fatal diseases. *Nature*, 422(6934):885–888, 2003.

1017 [39] Sema Nickbakhsh, Colette Mair, Louise Matthews, Richard Reeve, Paul CD  
1018 Johnson, Fiona Thorburn, Beatrix Von Wissmann, Arlene Reynolds, James  
1019 McMenamin, Rory N Gunson, et al. Virus–virus interactions impact the popu-  
1020 lation dynamics of influenza and the common cold. *Proceedings of the National  
1021 Academy of Sciences*, 116(52):27142–27150, 2019.

- 1022 [40] Neil Ferguson, Roy Anderson, and Sunetra Gupta. The effect of antibody-  
1023 dependent enhancement on the transmission dynamics and persistence of  
1024 multiple-strain pathogens. *Proceedings of the National Academy of Sciences*,  
1025 96(2):790–794, 1999.
- 1026 [41] Public Health Agency of Canada. Respiratory virus detections in  
1027 Canada. 2024. <https://www.canada.ca/en/public-health/services/surveillance/respiratory-virus-detections-canada.html>. Accessed Sep  
1028 4, 2024.
- 1030 [42] Centre for Health Protection. Detection of pathogens from respiratory spec-  
1031 imens. 2024. <https://www.chp.gov.hk/en/statistics/data/10/641/642/2274.html>. Accessed Nov 20, 2024.
- 1033 [43] Centre for Health Protection. Detection of gastroenteritis viruses from faecal  
1034 specimens. 2024. <https://www.chp.gov.hk/en/statistics/data/10/641/717/3957.html>. Accessed Nov 20, 2024.
- 1036 [44] Korea Disease Control and Prevention Agency. Acute respiratory infection,  
1037 Sentinel surveillance infectious diseases. 2024. <https://dportal.kdca.go.kr/pot/is/st/ari.do>. Accessed Nov 20, 2024.
- 1039 [45] Edward Goldstein, Sarah Cobey, Saki Takahashi, Joel C Miller, and Marc Lipsitch.  
1040 Predicting the epidemic sizes of influenza A/H1N1, A/H3N2, and B: a  
1041 statistical method. *PLoS medicine*, 8(7):e1001051, 2011.
- 1042 [46] Karline Soetaert, Thomas Petzoldt, and R Woodrow Setzer. Solving differential  
1043 equations in R: package deSolve. *Journal of statistical software*, 33:1–25, 2010.
- 1044 [47] R Core Team. *R: A Language and Environment for Statistical Computing*. R  
1045 Foundation for Statistical Computing, Vienna, Austria, 2023.
- 1046 [48] Sang Woo Park, Inga Holmdahl, Emily Howerton, Wenchang Yang, Rachel E  
1047 Baker, Gabriel A Vecchi, Sarah Cobey, C Jessica E Metcalf, and Bryan T Grenfell.  
1048 Interplay between climate, childhood mixing, and population-level suscep-  
1049 tibility explains a sudden shift in RSV seasonality in Japan. *medRxiv*, pages  
1050 2025–03, 2025.
- 1051 [49] Bob Carpenter, Andrew Gelman, Matthew D Hoffman, Daniel Lee, Ben  
1052 Goodrich, Michael Betancourt, Marcus A Brubaker, Jiqiang Guo, Peter Li,  
1053 and Allen Riddell. Stan: A probabilistic programming language. *Journal of  
1054 statistical software*, 76, 2017.
- 1055 [50] Stan Development Team. RStan: the R interface to Stan, 2024. R package  
1056 version 2.32.6.